RESEARCH ARTICLE

Iron Chelation Therapy Elicits Innate Immune Control of Metastatic Ovarian Cancer

Tito A. Sandoval[1,2], Camilla Salvagno[1,2], Chang-Suk Chae[1,2], Deepika Awasthi[1,2], Paolo Giovanelli[3], Matias Marin Falco[4], Sung-Min Hwang[1,2], Eli Teran-Cabanillas[1,2], Lasse Suominen[4], Takahiro Yamazaki[5], Hui-Hsuan Kuo[6], Jenna E. Moyer[6], M. Laura Martin[6], Jyothi Manohar[6], Kihwan Kim[7], Maria A. Sierra[3], Yusibeska Ramos[1], Chen Tan[1,2], Alexander Emmanuelli[1,2,3], Minkyung Song[8], Diana K. Morales[1], Dmitriy Zamarin[9], Melissa K. Frey[1,2], Evelyn Cantillo[1,2], Eloise Chapman-Davis[1,2], Kevin Holcomb[1,2], Christopher E. Mason[10,11,12], Lorenzo Galluzzi[2,5,6], Zhen Ni Zhou[1,2], Anna Vähärautio[4,13], Suzanne M. Cloonan[7,14], and Juan R. Cubillos-Ruiz[1,2,3]

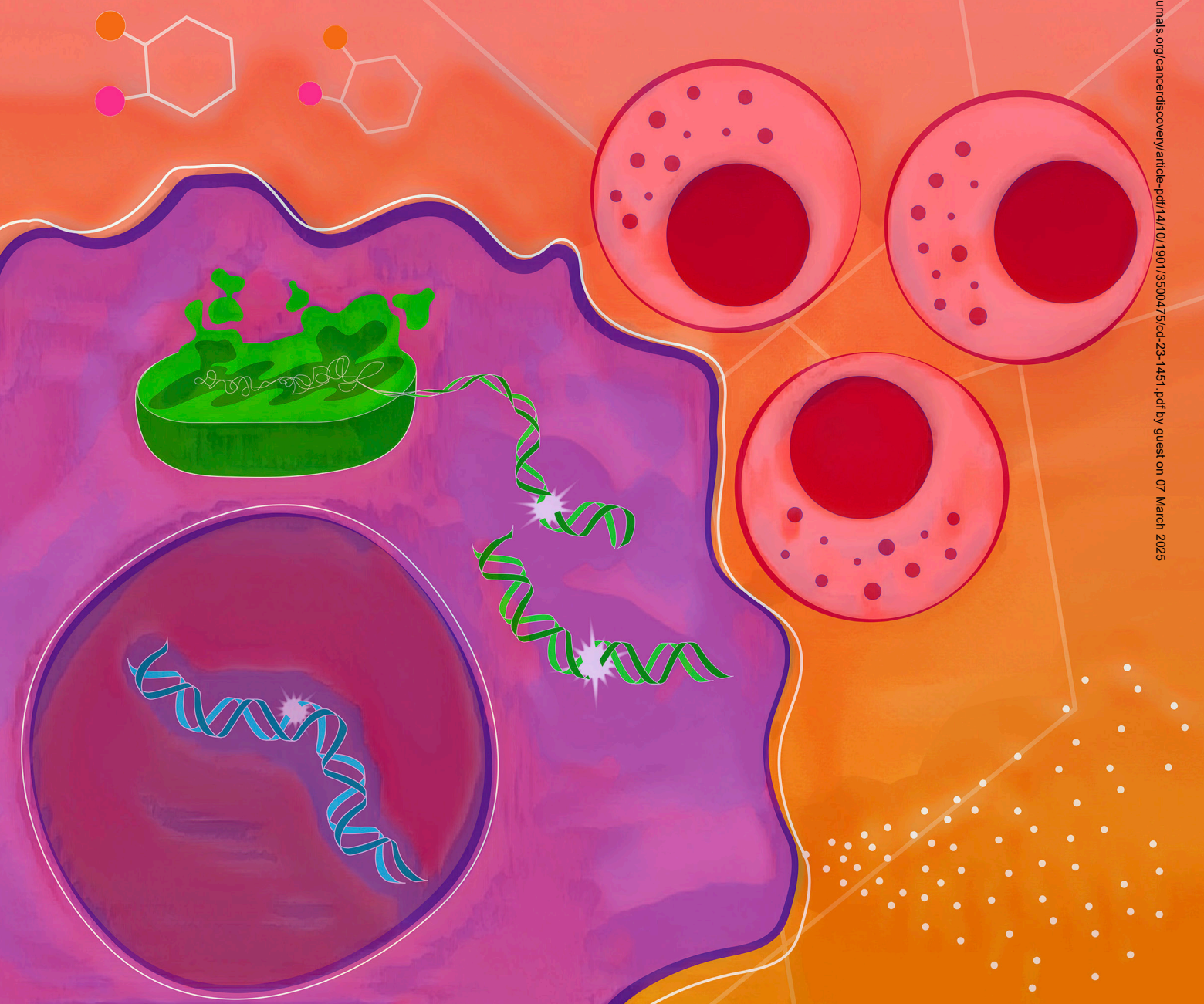

ABSTRACT Iron accumulation in tumors contributes to disease progression and chemoresistance. Although targeting this process can influence various hallmarks of cancer, the immunomodulatory effects of iron chelation in the tumor microenvironment are unknown. Here, we report that treatment with deferiprone, an FDA-approved iron chelator, unleashes innate immune responses that restrain ovarian cancer. Deferiprone reprogrammed ovarian cancer cells toward an immunostimulatory state characterized by the production of type-I IFN and overexpression of molecules that activate NK cells. Mechanistically, these effects were driven by innate sensing of mitochondrial DNA in the cytosol and concomitant activation of nuclear DNA damage responses triggered upon iron chelation. Deferiprone synergized with chemotherapy and prolonged the survival of mice with ovarian cancer by bolstering type-I IFN responses that drove NK cell-dependent control of metastatic disease. Hence, iron chelation may represent an alternative immunotherapeutic strategy for malignancies that are refractory to current T-cell–centric modalities.

SIGNIFICANCE: This study uncovers that targeting dysregulated iron accumulation in ovarian tumors represents a major therapeutic opportunity. Iron chelation therapy using an FDA-approved agent causes immunogenic stress responses in ovarian cancer cells that delay metastatic disease progression and enhance the effects of first-line chemotherapy.

See related commentary by Bell and Zou, p. 1771

INTRODUCTION

Iron is an essential micronutrient implicated in the homeostatic regulation of key cellular processes such as protein folding, mitochondrial respiration, DNA replication, proliferation, and metabolism (1). Disruption of iron homeostasis is associated with the initiation and maintenance of diverse pathologies, including cancer (2). Malignant cells have evolved strategies that enable them to thrive under adverse conditions, but at the cost of an elevated bioenergetic and metabolic demand that is highly dependent on iron utilization (3–5). Therefore, cancer cells use multiple mechanisms to ensure sustained iron availability, including overexpression of iron uptake and storage pathways, as well as downregulation of iron export proteins (3–5).

High-grade serous ovarian cancer (HGSOC), the most common and aggressive form of ovarian cancer (6), is resistant to standard treatments and refractory to current immunotherapies that harness the antitumor activity of T cells (6, 7). Disruptive therapeutic strategies are urgently needed in the clinic to improve the dismal survival of women with this disease. Interestingly, HGSOC is the prototypical iron-addicted malignancy (8, 9). Tumor specimens from patients with HGSOC demonstrate increased expression of transferrin receptor (TFR1), an iron importer, and decreased levels of the iron efflux pump ferroportin compared with normal ovarian tissue or low-grade serous ovarian tumors (8, 9). Previous studies indicate that iron augments the proliferative and invasive capacities of ovarian tumor–initiating cells and that ectopic overexpression of ferroportin in this population compromises peritoneal tumor growth in immunodeficient mice (8). Nonetheless, the therapeutic potential of targeting iron overload in metastatic ovarian cancer and the mechanistic basis through which iron chelation may represent a central vulnerability for these malignant cells have not been established.

Here, we sought to investigate the functional requirements of ovarian cancer cells on iron availability and evaluate the potential antiovarian cancer effects of the intracellular iron chelator deferiprone as a new therapeutic strategy that could

[1]Department of Obstetrics and Gynecology, Weill Cornell Medicine, New York, New York. [2]Sandra and Edward Meyer Cancer Center, Weill Cornell Medicine, New York, New York. [3]Weill Cornell Graduate School of Medical Sciences, New York, New York. [4]Research Program in Systems Oncology, Research Programs Unit, Faculty of Medicine, University of Helsinki, Helsinki, Finland. [5]Department of Radiation Oncology, Weill Cornell Medicine, New York, New York. [6]Caryl and Israel Englander Institute for Precision Medicine, Weill Cornell Medicine, New York, New York. [7]Division of Pulmonary and Critical Care Medicine, Department of Medicine, Weill Cornell Medicine, New York, New York. [8]Departments of Integrative Biotechnology and of Biopharmaceutical Convergence, University of Suwon, Suwon, Korea. [9]Tisch Cancer Institute, Icahn School of Medicine at Mount Sinai, New York, New York. [10]The HRH Prince Alwaleed Bin Talal Bin Abdulaziz Alsaud Institute for Computational Biomedicine, Weill Cornell Medicine, New York, New York. [11]Department of Physiology and Biophysics, Weill Cornell Medicine, New York, New York. [12]The WorldQuant Initiative for Quantitative Prediction, Weill Cornell Medicine, New York, New York. [13]Foundation for the Finnish Cancer Institute, Helsinki, Finland. [14]School of Medicine, Trinity Biomedical Sciences Institute, Trinity College, Dublin, Ireland.

Current address for Chang-Suk Chae: Research Institute, National Cancer Center, Goyang, Republic of Korea; current address for Eli Teran-Cabanillas, Facultad Ciencias de la Nutrición y Gastronomía, Universidad Autónoma de Sinaloa, Culiacan Rosales, Sinaloa, Mexico; and current address for Zhen Ni Zhou, Department of Obstetrics and Gynecology, University of Michigan. Ann Arbor, Michigan.

Corresponding Author: Juan R. Cubillos-Ruiz, Microbiology and Immunology, Well Cornell Medicine, New York, NY 10065. E-mail: jur2016@med.cornell.edu

Cancer Discov 2024;14:1901–21

doi: 10.1158/2159-8290.CD-23-1451

be rapidly translated into a clinical setting given the widespread use of this FDA-approved agent for the treatment of patients with transfusional iron overload (10).

Our study reveals that treatment with deferiprone blocks mitochondrial respiration while concurrently activating nuclear DNA damage responses in ovarian cancer cells. This dual effect unleashes innate immune responses driven by type-I IFN signaling and NK cells that impair disease progression and enhance the efficacy of first-line chemotherapy. Our findings suggest that deferiprone might be repurposed as a new immunotherapeutic agent to treat patients with metastatic ovarian cancer, which is generally insensitive to T-cell–based immunotherapy (6, 7).

RESULTS

Expression of Iron-Related Gene Signatures is Associated with Poor Prognosis in Patients with HGSOC

Ovarian tumors demonstrate a distinctive iron-dependent phenotype (8), but whether the expression status of iron-related gene signatures in HGSOC specimens may predict prognosis is unknown. We exploited published scRNA-seq data generated from metastatic tumor samples of patients with HGSOC (11) and analyzed the expression of gene programs involved in iron homeostasis, transport, accumulation, and function. Compared with immune and stromal cells in the same microenvironment, EOCs demonstrated a significant increase in diverse iron-related gene signatures, especially the iron sequestration signature (Fig. 1A). EOCs also exhibited elevated scores for iron-related gene signatures and compared with the main cell type of origin for this malignancy, the epithelial (secretory) cells present in the fallopian tube of women without cancer (Fig. 1B; ref.12). Importantly, no differences in the expression of these gene sets were observed in epithelial cells from noncancerous fallopian tube compared with other cell types present in the same specimens (Fig. 1C). These data indicate that iron-related gene signatures are preferentially overexpressed in malignant cells of the ovarian tumor microenvironment. Further analysis of deconvoluted bulk RNA-seq and clinical data from 292 patients with HGSOC in TCGA (13, 14) revealed that the presence of gene signatures involved in transmembrane iron transport or import across the plasma membrane, as well as high scores of a ferrous iron binding gene signature in cancer cells, were associated with reduced overall survival (OS) in patients with HGSOC (Fig. 1D).

Women with advanced ovarian cancer often present with accumulation of ascites, a malignant and immunosuppressive peritoneal fluid associated with drug resistance and metastatic disease (15). Proteomic analyses of patient-derived ascites samples revealed that this fluid is enriched for proteins implicated in iron transport and metabolism, including serotransferrin (TF), α1-antitrypsin (SERPINA1), ceruloplasmin (CP), the hepcidin-binding protein α2-macroglobulin (A2M), and apolipoprotein B100 (APOB), among several others (Fig. 1E; Supplementary Tables S1 and S2). We also found that ~50% of the clinical ascites samples analyzed contained total iron levels higher than the range typically found in human serum (Fig. 1F). Unbiased analysis of cytokines, chemokines, and growth factors in the same samples further indicated that the total iron concentration in this fluid positively correlated with the levels of multiple tumorigenic mediators such as vascular endothelial growth factor A (VEGFα), C-X-C motif chemokine ligand 5 (ENA78, CXCL5), C-X-C motif chemokine ligand 8 (CXCL8, IL8), platelet-derived growth factor receptor beta (PDGF), and C-C motif chemokine ligand 7 (MCP3, CCL7; Fig. 1G; refs. 16–19).

These data uncover that iron-related gene signatures are selectively overexpressed by malignant cells within metastatic HGSOC tumors and that the expression status of iron transport–related gene programs are associated with reduced patient survival. In addition, our analyses indicate that the ascites may function as a local source of iron that is readily available to ovarian cancer cells overexpressing iron-related transporters.

Therapeutic Effects of Iron Chelation in Ovarian Cancer Hosts

We sought to determine the potential antitumor effects of targeting iron accumulation in mouse models of metastatic ovarian cancer. To this end, we used the orthotopic ID8-*Defb29/Vegfa* model, which engenders a highly chemoresistant and immunosuppressive peritoneal carcinomatosis that recapitulates the advanced stages of human ovarian cancer (20–22). Consistent with our observations in patient specimens, we found progressive accumulation of iron in the peritoneal cavity of mice developing ID8-*Defb29/Vegfa* tumors (Fig. 2A). scRNA-seq analyses also revealed that diverse malignant cell states residing in this anatomical location present high enrichment scores for several iron-related gene signatures, compared with immune and stromal cell types present in the same milieu (Fig. 2B and C). Thus, we evaluated whether the dietary iron levels may influence metastatic disease progression. To this end, mice were intraperitoneally challenged with parental ID8 ovarian tumors, and 3 days later, isocaloric diets containing low, normal, or high amounts of iron (3, 45, or 350 ppm, respectively) were provided *ad libitum* until endpoint. Altering the iron content of diet did not affect the progression of these peritoneal tumors, as all experimental groups demonstrated similar survival rates (Supplementary Fig. S1A). Hence, we sought to assess whether blocking iron accumulation in the ovarian cancer microenvironment using a pharmacological approach might elicit therapeutic effects.

Deferiprone is an FDA-approved intracellular iron chelator used to treat transfusional iron overload in patients with β-thalassemia (10, 23). This agent has also been tested in patients with diverse neurological disorders characterized by dysregulated iron accumulation (NCT01539837, NCT03234686, NCT02728843, NCT00530127, NCT02164253, NCT00943748, and NCT02174848), but its potential activity against ovarian cancer has not been evaluated. Due to the enrichment of multiple iron-related gene signatures in human EOCs (Fig. 1A–C) and in chemoresistant malignant cells naturally found in mice bearing ID8-*Defb29/Vegfa* ovarian tumors (Fig. 2C), we sought to evaluate the therapeutic effects of deferiprone in this model when administered alone or in combination with cisplatin, which is the first-line chemotherapy used in the clinic for this disease (Fig. 2D). Consistent with the intrinsic chemoresistant nature of ID8-based tumors (20, 21, 24), cisplatin had a minor impact on disease progression (Fig. 2E–H) and minimally

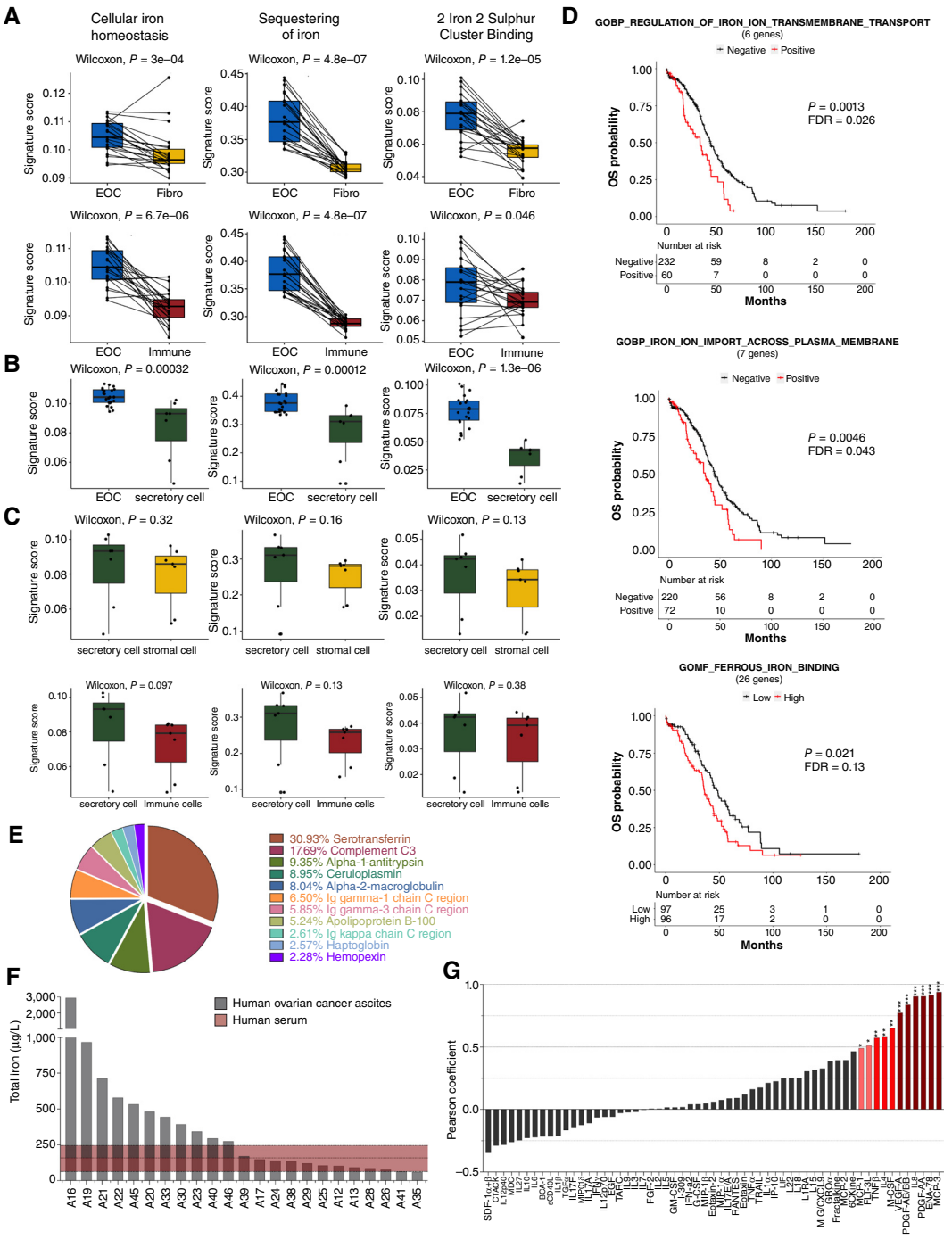

Figure 1. Status of iron-related gene signatures and factors in human HGSOC. **A,** Expression of iron-related gene signatures in human HGSOC. Box plots indicate the average iron signature scores from scRNA-seq analyses. EOCs are shown in blue, whereas fibroblasts (Fibro) and immune cells are shown in yellow and red, respectively. Pairwise Wilcoxon tests were conducted, and exact *P* values are shown ($n = 22$ independent specimens). **B,** Comparative analysis of iron-related gene signatures in human HGSOC vs. normal fallopian tube samples. Box plots indicate the average iron signature scores from scRNA-seq analyses. EOCs are shown in blue ($n = 22$ independent specimens), normal secretory cells showed in green ($n = 8$ independent specimens). **C,** Comparative analysis of the indicated iron-related gene signatures in noncancerous fallopian tube ($n = 8$ independent specimens). Unpaired Wilcoxon tests were conducted, and exact *P* values are shown. **D,** Status of the indicated iron-related gene signatures and patient outcome. Survival analysis was based on deconvoluted bulk RNA-seq from TCGA data. Curated human gene sets were used to assess iron-related features. Patients with negative or low expression were compared with those with positive or high expression of signature scores. Survival analysis was performed with Cox proportional hazards model, and results are adjusted for FDR. **E,** Proteomic analysis of cell-free ascites samples obtained from patients with ovarian cancer. The percentage distribution of the major proteins is shown. **F,** Iron concentration in cell-free ascites. The range of iron concentrations in six serum samples from cancer-free donors is depicted in red. Ascites codes represent independent patients with ovarian cancer. **G,** Correlation of iron content and concentration of diverse soluble factors in patient-derived ascites. Pearson correlation test was conducted in all patients analyzed. Statistically significant correlation coefficients are highlighted in red. Significance levels are marked in the plots, *, $P < 0.05$; **, $P < 0.01$; ***, $P < 0.001$; $n = 23$ independent human ascites samples. BioRender.com

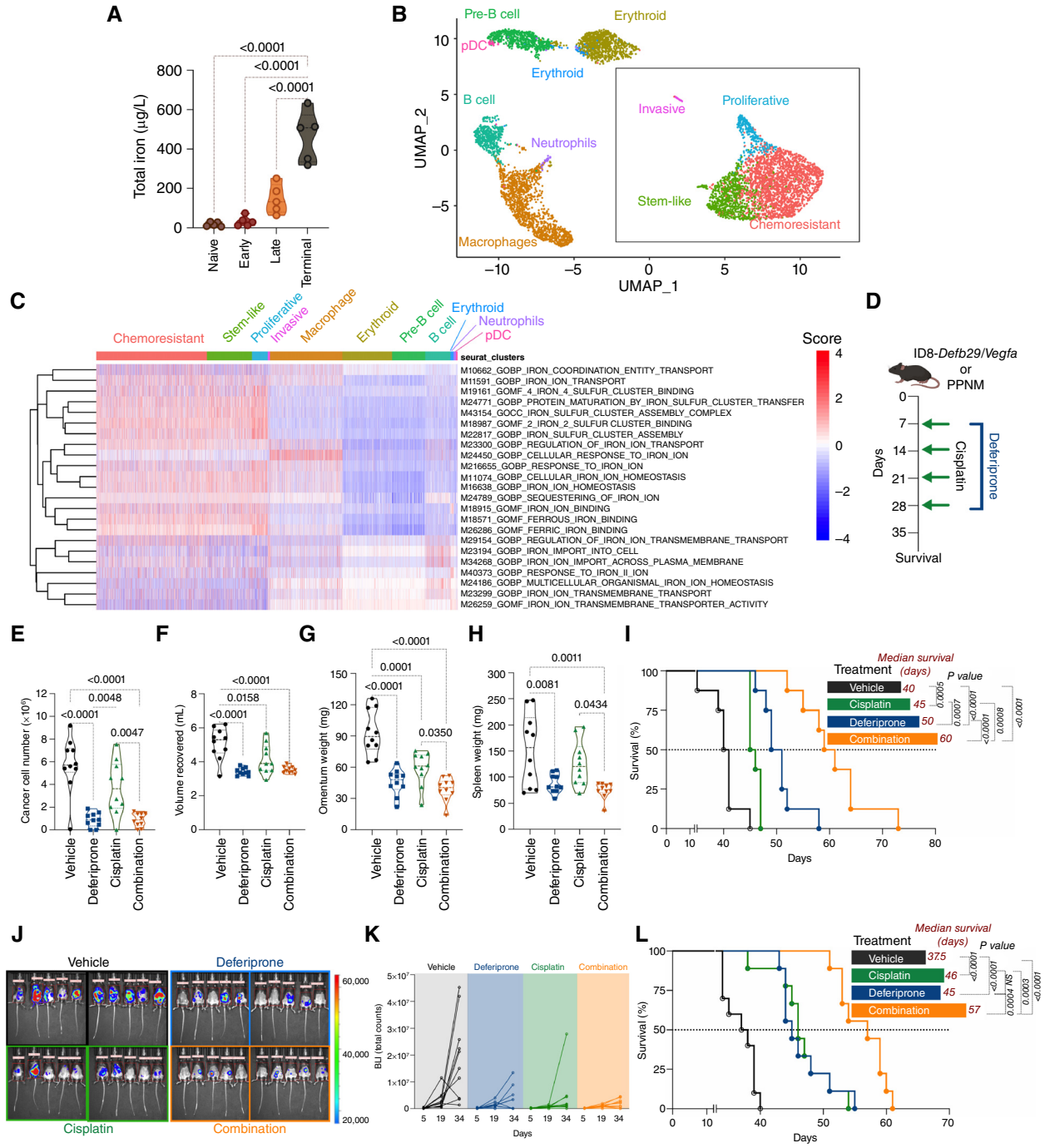

Figure 2. Iron chelation therapy extends survival in mouse models of ovarian cancer. **A,** Total iron in peritoneal lavage or ascites samples of female mice with ID8-*Defb29/Vegfa* tumors at different disease stages. **B,** Cluster analysis of cells found in the ascites of mice with late-stage metastatic disease. Mice were implanted with ID8-*Defb29/Vegfa* tumors and after 35 days of tumor progression, the cellular fraction of the ascites was analyzed by scRNA-seq. Unbiased cluster analysis (UMAP projection) of cells ($n = 6{,}502$) showing 11 distinct clusters. Ovarian cancer cells are highlighted within the square. **C,** Enrichment analysis of iron-related gene signatures in each cluster. Heatmap of single-sample Gene Set Enrichment Analysis showing scores for 23 iron-related gene signatures for each cell, grouped by the clusters defined in **B**. **D,** Schematic representation of treatment regimens. Mice were implanted intraperitoneally with ID8-*Defb29/Vegfa* or PPNM cancer cells and then treated as indicated. **E–H,** Disease features in mice bearing ID8-*Defb29/Vegfa* tumors analyzed 48 hours after the last treatment (day 30 of tumor progression). **E,** Number of peritoneal cancer cells. **F,** Volume of ascites recovered. **G,** Omentum weight as indicator of tumor burden in this organ. **H,** Tumor-induced splenomegaly. Violin plots with individual data points are shown. One-way ANOVA with Tukey multiple comparison test was applied, and exact *P* values are displayed. **I,** OS rates for mice bearing ID8-*Defb29/Vegfa* tumors. Log-rank (Mantel–Cox) test was used, and *P* values are provided ($n = 8$). Data are representative of at least three independent experiments with similar results. **J–L,** Metastatic progression and survival analysis in mice bearing PPNM-based HGSOC. **J,** Bioluminescence imaging (BLI) at day 34. **K,** Quantification of peritoneal tumor burden at different time points. **L,** Kaplan–Meier survival curves. Log-rank (Mantel–Cox) test was used, and *P* values are shown ($n = 9$–10 mice/group). (Created with BioRender.com.)

extended OS in host (Fig. 2I). By contrast, deferiprone administration was sufficient to decrease the number of malignant cells in the peritoneal cavity while simultaneously reducing ascites accumulation, omental metastases, and tumor-induced splenomegaly (Fig. 2E–H). Strikingly, tumor-bearing mice receiving deferiprone demonstrated a ~25% increase in their median survival rates in comparison with untreated mice, and this therapeutic benefit was doubled upon combination treatment with cisplatin (Fig. 2I). The therapeutic effects of deferiprone were dose dependent (Supplementary Fig. S1B), and a comparable survival benefit was observed when the drug was administered either intraperitoneally or orally (Supplementary Fig. S1C). *In vivo*, deferiprone administration significantly decreased the intracellular iron levels in ovarian cancer cells (Supplementary Fig. S1D) and prevented the accumulation of total and heme-bound iron at peritoneal tumor sites (Supplementary Fig. S1E).

To further confirm these therapeutic findings, we used the *Trp53*^{R172H}*Pten*$^{-/-}$*Nf1*$^{-/-}$*Myc*^{OE} (PPNM) model of high-grade serous tubo-ovarian carcinoma that carries the most common genetic abnormalities present in human HGSOC (25). In this independent system, deferiprone also induced significant antitumor effects characterized by reduced peritoneal carcinomatosis (Fig. 2J and K) and increased host survival (Fig. 2L), which was drastically augmented upon combination with cisplatin (Fig. 2L). Importantly, mice bearing ID8 or PPNM metastatic ovarian tumors did not show major signs of toxicity or weight loss during treatment with deferiprone, both as a single agent and in combination with cisplatin (Supplementary Fig. S1F and S1G).

Hence, we conclude that ovarian cancer progression is characterized by iron accumulation in the peritoneal cavity and an enrichment of iron-related gene signatures in malignant cells present in this milieu. Moreover, treatment with deferiprone induces significant responses against ovarian cancer that enhance the effects of first-line chemotherapy in two independent mouse models of metastatic disease.

Treatment with Deferiprone Promotes NK Cell–Dependent Control of Metastatic Ovarian Cancer

We next sought to determine whether deferiprone administration impacts the aggressive microenvironment of metastatic ovarian cancer. To this end, female mice bearing peritoneal ID8-*Defb29/Vegfa* tumors were treated with deferiprone, alone or in combination with cisplatin, as shown in Fig. 2D, and mice were euthanized 24 hours after the last treatment for flow cytometry–based analysis of peritoneal immune infiltrates (Supplementary Fig. S2) and histological assessment of metastatic omental lesions. When given alone or in combination with cisplatin, deferiprone increased the proportion of peritoneal macrophages in tumor-bearing mice (Supplementary Fig. S3A). Deferiprone also augmented the percentage of monocytes in the peritoneum while modestly altering dendritic cell (DC), B-cell, and T-cell infiltration (Supplementary Fig. S3B–S3F). The therapeutic effects of deferiprone, alone or in combination with cisplatin, remained unaltered in *Rag2*$^{-/-}$ mice that lack T and B cells (Supplementary Fig. S3G and S3H), demonstrating that the observed survival benefit was not mediated by improved adaptive immunity. Strikingly, iron chelation using deferiprone significantly increased the proportion of NK cells in the peritoneal cavity (Fig. 3A) while eliciting robust NK cell infiltration into metastatic omental lesions (Fig. 3B and C; Supplementary Fig. S4A). These changes were specific to malignant sites, as negligible changes in splenic NK cell proportions were found in treated mice (Supplementary Fig. S4B). To define whether NK cells mediated the therapeutic effects of deferiprone, we used antibody-mediated depletion of this population in tumor-bearing mice (Fig. 3D). NK cell ablation did not affect the OS rates of mice receiving vehicle control or cisplatin (Fig. 3E; Supplementary Fig. S4C), yet it reduced the therapeutic effects of deferiprone when administered alone and, more drastically, upon combination with cisplatin (Fig. 3F and G; Supplementary Fig. S4C). These data reveal that, at least in mice, deferiprone elicits major T- and B-cell–independent therapeutic responses against metastatic ovarian cancer that are partly mediated by NK cells.

Deferiprone Induces Immunostimulatory Gene Programs in Ovarian Cancer Cells

We sought to dissect the mechanisms mediating the surprising immunomodulatory effects of deferiprone in ovarian cancer hosts. To this end, we first identified the main molecular processes that this agent altered in ovarian cancer cells. Viability assays indicated that deferiprone did not induce direct cytotoxic effects at concentrations below 100 μmol/L in murine ovarian cancer cell lines, even when exposed to the compound for up to 48 hours (Supplementary Fig. S5A). Similar results were observed when multiple human ovarian cancer cell lines were used in these experiments (Supplementary Fig. S5B). In addition, the combination of deferiprone and cisplatin did not exert synergistic cytotoxicity in these *in vitro* systems (Supplementary Fig. S5C). Hence, we evaluated whether deferiprone could alter global gene expression profiles in ovarian cancer cells. RNA-seq analyses identified 995 differentially expressed genes, of which 97 were downregulated and 898 were upregulated, in ID8-*Defb29/Vegfa* cells exposed to deferiprone for 12 hours compared with their control counterparts treated with vehicle [fold change (FC) > 2.0; FDR < 5%; P value < 0.05; Supplementary Table S3]. We next examined the differentially expressed genes by IPA to identify potential upstream regulators mediating the observed transcriptomic changes. As expected, the transferrin receptor emerged as a top regulator whose downstream target genes were inhibited upon deferiprone exposure (Fig. 4A). Surprisingly, gene programs controlled by immunosuppressive TGFβ, IL10, and prostaglandin signaling (PTGER4) were repressed in deferiprone-treated cancer cells (Fig. 4A), whereas diverse elements mediating the production and biological activity of type-I IFN (MYD88, STING1, TBK1, IRF3, IFNB1, IFNAR1, and STAT1) were enriched in cells responding to deferiprone (Fig. 4A). Hypoxia inducible factor 1 subunit alpha (HIF1A) and activating transcription factor 4 (ATF4), which have been shown to coordinate mitochondrial stress responses (26, 27), also emerged as upstream regulators activated by deferiprone (Fig. 4A). Interestingly, gene networks controlled by PARP1 and NCOA2, which orchestrate DNA damage responses (DDR) and maintain genome integrity, were also predicted to be activated in ovarian cancer cells

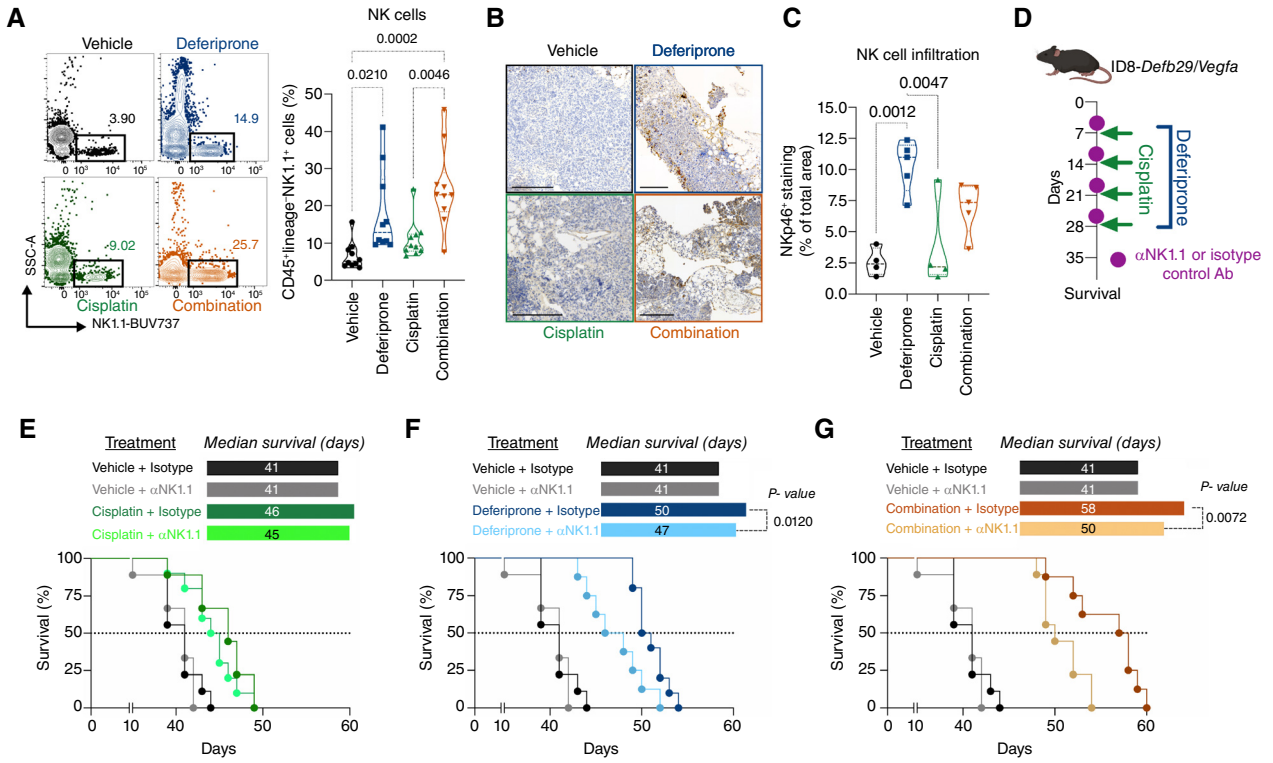

Figure 3. Treatment with deferiprone elicits NK cell–mediated control of ovarian cancer. **A–C,** Female mice bearing ID8-*Defb29/Vegfa* tumors were treated as shown in Fig. 2D. Peritoneal lavage samples (**A**) and omental tissue (**B** and **C**) were analyzed at day 30 of tumor progression. **A,** Representative FACS plots and global violin plots showing the proportion of NK cells in the peritoneal cavity ($n = 10$/group). **B,** Representative images for NKp46 staining in the omentum. Scale bar, 200 μm. **C,** NKp46 expression was quantified as the percentage of tissue stained and normalized to total tissue area ($n = 4$–5 mice/group). **D,** Schematic representation of treatment regimens using NK cell–depleting antibodies. **E–G,** Kaplan–Meier survival curves for the indicated treatment groups ($n = 8$–10 mice/group). Median survival and exact *P* values for the log-rank (Mantel–Cox) test comparing groups treated with isotype vs. NK cell–depleting antibodies are shown. **E–G,** Survival curves were derived from the same experiment, but specific comparisons are shown to highlight individual effects. All statistical comparisons are described in Supplementary Fig S4C. (Created with BioRender.com.)

treated with deferiprone (Fig. 4A). Further inspection of the differentially expressed genes based on these analyses revealed that deferiprone upregulated several transcripts implicated in cytokine-to-cytokine receptor interactions, type-I IFN signaling, mitophagy, and NK cell activation (Fig. 4B). Of note, within these categories, we observed marked overexpression of *Fas* and *Tnfrsf10b* (encoding the death receptors FAS and DR5, respectively; ref. 28); type-I IFN–stimulated genes (ISG) such as *Rsad2*, *Cxcl10*, *Ddx58*, and *Mx1*; mitochondrial stress markers (*Pink1*, *Atgb9*, *Bnip3*, and *Ddit4*), as well as genes encoding diverse NKG2D ligands (*Ulbp1/MULT1* and *H60b*; Fig. 4B). Indeed, *in vitro* deferiprone exposure rapidly upregulated surface expression of DR5 while triggering a dose- and time-dependent overexpression of MULT1 on multiple ovarian cancer cell lines (Supplementary Fig. S5D–S5F).

To validate these findings *in vivo*, female mice with established ID8-*Defb29/Vegfa* tumors were treated with vehicle control or deferiprone for 3 consecutive days, and metastatic cancer cells were sorted from peritoneal lavage samples 24 hours after the last treatment. Deferiprone administration upregulated *Tnfrsf10b*, *Fas*, *Ulbp1*, *Ddit4*, and multiple type-I IFN–related genes such as *Ifna*, *Ifnb1*, *Isg15*, and *Ifit1* in malignant cells (Fig. 4C). Tumor-bearing mice treated with deferiprone also showed surface overexpression of DR5 on ovarian cancer cells (Fig. 4D) and increased levels of IFNβ1 and the type-I IFN–dependent chemokines CCL12, CCL20, and CX3CL1 (Fig. 4E) in the peritoneal cavity, compared with their control counterparts receiving vehicle. These results were further validated using primary cultures of ovarian cancer organoids ($n = 4$) generated from patients with advanced disease (Supplementary Table S4). Notably, deferiprone exposure triggered dose-dependent overexpression of *ATG9B*, *TNFRSF10B*, type-I IFN transcripts, ISGs, and genes encoding NKG2D ligands such as *MICA*, *MICB*, and *ULBP1-3* in 75% of the independent organoids analyzed (Fig. 4F). Similar effects were observed when diverse human ovarian cancer cell lines were used in these experiments (Supplementary Fig. S6A and S6B).

Hence, deferiprone-treated ovarian cancer cells upregulate gene programs involved in mitochondrial stress and DNA damage responses while concurrently overexpressing factors that promote NK cell activation and type-I IFN production and sensing.

Deferiprone Triggers Innate Immune Signaling in Malignant Cells

Iron is an essential element involved in diverse cellular homeostatic and metabolic processes (29). Enzymes containing iron–sulfur (Fe-S) clusters play a crucial role in the regulation

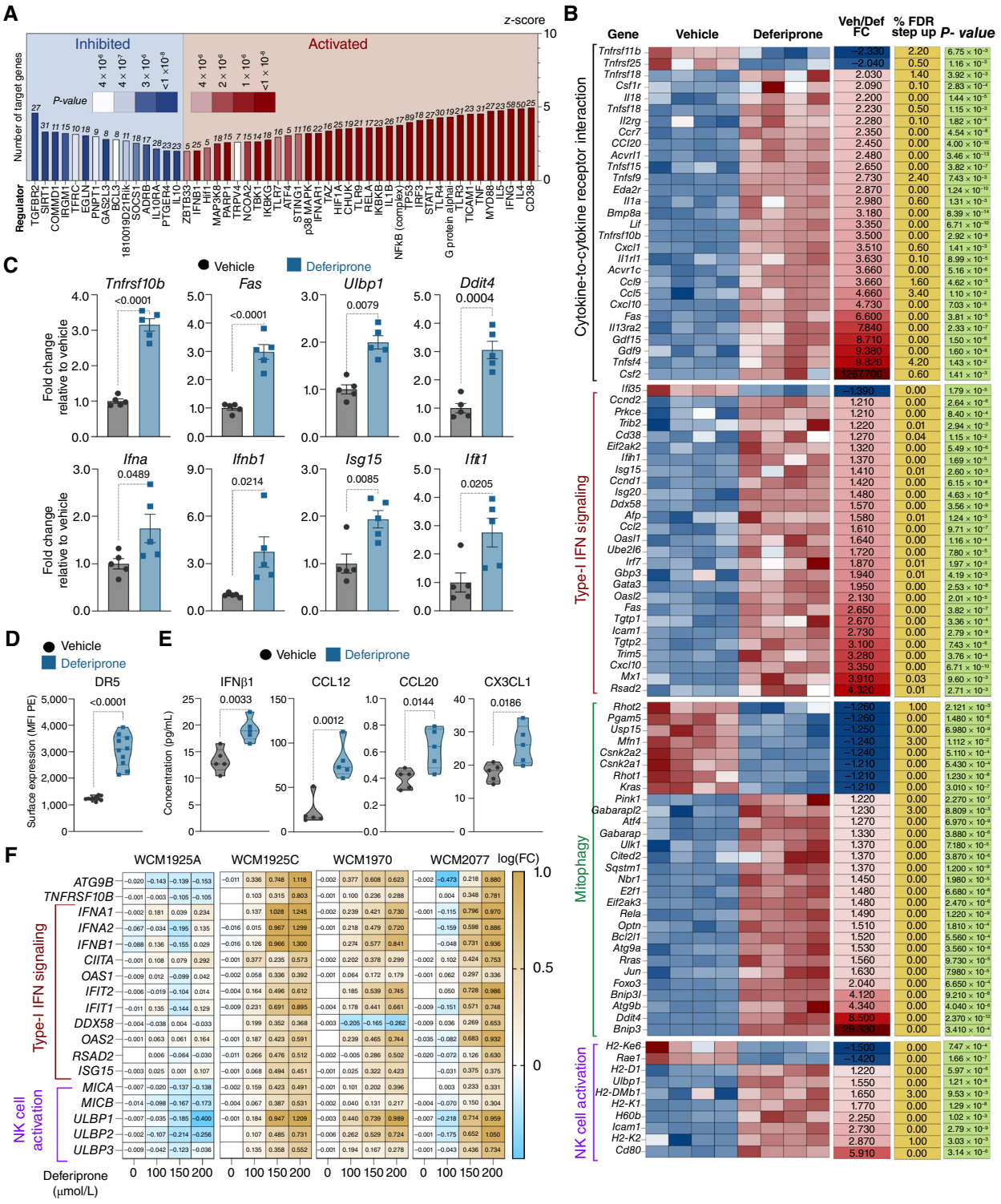

Figure 4. Deferiprone exposure induces innate immune gene programs in ovarian cancer cells. ID8-*Defb29/Vegfa* cells were treated with deferiprone or vehicle control for 12 hours, and global transcriptional profiles were analyzed by RNA-seq ($n = 4$/group). **A,** Predicted upstream regulator analysis. **B,** Heat maps for differentially expressed genes within the indicated categories showing FC, FDR, and exact *P* values. **C–E,** Mice bearing ID8-*Defb29/Vegfa* tumors for 21 days received an i.p. dose of deferiprone or vehicle control, and peritoneal lavage samples were analyzed 24 hours later. **C,** Expression of the indicated genes in sorted cancer cells was analyzed by qRT-PCR ($n = 5$ mice/group). **D,** Surface levels of DR5 on cancer cells analyzed by FACS ($n = 10$ mice/group). **E,** Concentration of the indicated factors on cell-free peritoneal lavage samples ($n = 5$ mice/group). Unpaired Student *t* test was used to compare vehicle vs. deferiprone groups. **F,** Patient-derived ovarian cancer organoids were treated with deferiprone for 72 hours and expression of the indicated genes was analyzed by qRT-PCR. Colors indicate log FC upon deferiprone treatment, and this experiment was repeated three independent times with similar results. BioRender.com

of mitochondrial electron transport, respiration, and metabolism (30). Iron chelation has been documented to cause mitochondrial anomalies in malignant cells (31), but the immunomodulatory consequences of this process are unknown. Importantly, disruption of mitochondrial activity and/or integrity can ignite cell-intrinsic inflammatory programs via activation of cytosolic innate immune sensors that detect the leakage of mitochondrial DNA (mtDNA; ref. 32). Since our transcriptomic analyses indicated upregulation of mitochondrial stress responses in deferiprone-treated cancer cells (Fig. 4A and B), we sought to determine whether mitochondrial perturbations provoked by this iron chelator mediated the observed induction of type-I IFN and NK cell–activating factors.

Ovarian cancer cells overloaded with ammonium iron (II) sulfate demonstrated severe mitochondrial iron accumulation, which was effectively mitigated by treatment with deferiprone (Supplementary Fig. S7A and S7B). Hence, we examined whether deferiprone could affect mitochondrial respiration in ovarian cancer cells. Assessment of OCR using extracellular flux analyzers determined that deferiprone rapidly caused a dose-dependent decrease in their basal respiration, maximal respiration, proton leak, coupling efficiency, and ATP production (Fig. 5A and B). Deferiprone also abolished the activity of mitochondrial aconitase, an iron–sulfur–containing enzyme crucial for cellular homeostasis and metabolism (Fig. 5C). Furthermore, malignant cells treated with deferiprone exhibited increased amounts of mtDNA in their cytosol, as evidenced by quantification of DNA fragments corresponding to the mitochondrial cytochrome c oxidase (*mt-Cox1*) gene (Fig. 5D). Hence, deferiprone readily perturbs mitochondrial homeostasis and causes leakage of mtDNA into the cytosol of ovarian cancer cells.

mtDNA is sensed in the cytoplasm by the cyclic GMP-AMP synthase (cGAS)–stimulator of interferon genes (STING) system (33), which leads to TBK1-mediated phosphorylation of the interferon regulatory factor 3 (IRF3) that enables the expression of genes encoding type-I IFN (34, 35). Thus, we next investigated whether activation of this innate immune pathway by leaked mtDNA mediated the induction of type-I IFN genes in deferiprone-treated cancer cells. Deferiprone failed to induce *Ifnb1* and the prototypical ISG *Mx1* in ρ^0 ovarian cancer cells devoid of mtDNA (Supplementary Fig. S7C and S7D; ref. 36), supporting a role for mtDNA in this process. We also observed robust IRF3 phosphorylation in deferiprone-treated ovarian cancer cells (Supplementary Fig. S7E), further suggesting activation of the cGAS-STING-IRF3 axis upon iron chelation. To functionally validate the role of this pathway, we used the STING inhibitor H151 (37) and also generated isogenic ovarian cancer cell lines in which IRF3 expression was abrogated via CRISPR-Cas9 (Supplementary Fig. S7F and S7G). Notably, suppressing STING activation (Fig. 5E) or ablating IRF3 (Fig. 5F) prevented the induction of *Ifnb1* and *Mx1* transcripts in ovarian cancer cells treated with deferiprone. These results indicate that deferiprone compromises mitochondrial respiration and causes the release of mtDNA into the cytosol, evoking type-I IFN expression in ovarian cancer cells via the cGAS-STING-IRF3 axis. Intriguingly, however, we observed that targeting STING or IRF3 did not affect the induction of *Tnfrsf10b* (DR5) or *Ulbp1* (MULT1) in deferiprone-exposed ovarian cancer cells (Supplementary Fig. S7H and S7I), suggesting an independent, yet concurrent immunostimulatory mechanism ignited by this iron chelator.

Multiple DNA repair enzymes use iron as a central cofactor (38). Disruption of iron metabolism can therefore perturb DNA synthesis and repair, leading to the activation of the DDR (39). ATM and ATR govern the DDR by activating their downstream checkpoint kinases CHK1 and CHK2 (40, 41). Of note, these pathways have been shown to mediate the induction of NKG2D ligands on cancer cells undergoing canonical DNA damage (42). We sought to determine if the DDR mediated the induction of DR5 and MULT1 in deferiprone-exposed ovarian cancer cells. Rapid phosphorylation of CHK1 was observed in ovarian cancer cells treated with deferiprone (Supplementary Fig. S7J). Most importantly, inhibiting ATR or CHK1/2 impaired the surface overexpression of DR5 and MULT1 in ovarian cancer cells responding to deferiprone, whereas ATM inhibition had negligible effects in this system (Fig. 5G–J). Similar effects were observed when ovarian cancer cells were exposed to the classical DNA polymerase inhibitor aphidicolin (Supplementary Fig. S7K–S7N; ref. 43).

Collectively, these results indicate that chelating intracellular iron with deferiprone evokes two mutually reinforcing immunostimulatory mechanisms in ovarian cancer cells: the leakage of mtDNA that drives type-I IFN production via the cGAS-STING-IRF3 axis and DDR activation that bolsters surface expression of NK cell–activating factors such as DR5 and MULT1.

Deferiprone-Induced Type-I IFN Drives Protective NK Cell Responses by Enhancing IL15 Expression in Tumor-Associated DCs

We next evaluated whether the immunotherapeutic effects of deferiprone were indeed mediated by increased type-I IFN signaling in the ovarian cancer microenvironment. To this end, female mice bearing peritoneal ID8-*Defb29/Vegfa* tumors were treated with deferiprone as a single agent or in combination with cisplatin, and mice further received antibodies blocking the IFN alpha and beta receptor subunit 1 (IFNAR1) or its corresponding isotype control (Supplementary Fig. S8A). Hindering type-I IFN signaling by this approach did not affect the OS rates of ovarian cancer–bearing mice left untreated or receiving cisplatin (Fig. 6A; Supplementary Fig. S8B), yet it markedly reduced the therapeutic benefit conferred by deferiprone when administered alone and in combination with cisplatin (Fig. 6B and C; Supplementary Fig. S8B). Hence, type-I IFN signaling operates as a crucial driver of the antiovarian cancer effects induced by this intracellular iron chelator.

Type-I IFN is key for the optimal activation, expansion, and antitumor function of NK cells in cancer (44–46). We hypothesized that type-I IFN elicited by deferiprone promoted the observed NK cell accumulation at metastatic tumor sites. To test this, we focused on deferiprone and cisplatin cotreatment, as it induced maximal immunotherapeutic effects mediated by NK cells (Fig. 3G). Antibody-mediated blockade of IFNAR1 prevented NK cell accumulation at tumor sites in response to combination therapy (Supplementary Fig. S8C and S8D; Fig. 6D), establishing a major protective role for the

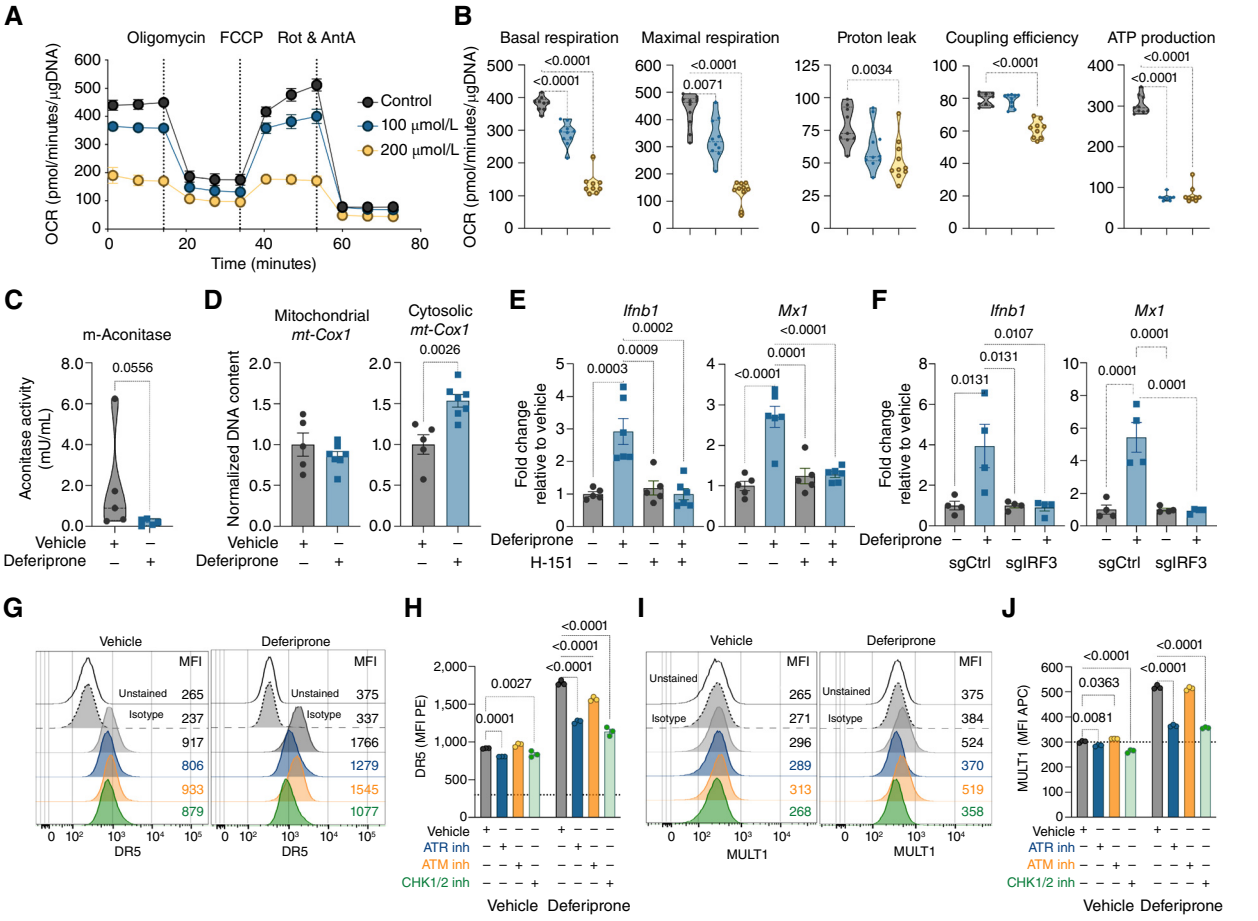

Figure 5. Innate immune signaling triggered by deferiprone in ovarian cancer cells. **A** and **B,** ID8-*Defb29/Vegfa* cells were treated with deferiprone or vehicle control for 6 hours and mitochondrial respiration was assessed thereafter. **A,** Representative OCR plots where each time point represents the mean ± SEM. **B,** Analysis of the indicated mitochondrial respiration parameters using violin plots with all data points, median, and quartiles ($n = 9$–10 per condition). **C,** Female mice developing metastatic ID8-*Defb29/Vegfa* tumors for 28 days received one dose of deferiprone (150 mg/kg), and 8 hours later, tumor cells were sorted from peritoneal lavage. Mitochondrial aconitase activity was measured thereafter ($n = 5$ independent mice). **D,** ID8-*Defb29/Vegfa* cells were treated with deferiprone (100 µmol/L) for 3 hours. Cytosolic or mitochondrial DNA were simultaneously extracted, and the abundance of the indicated genes was analyzed by qPCR ($n = 5$–7 independent samples). **E,** Expression of the indicated genes in deferiprone-exposed ID8-*Defb29/Vegfa* cells pretreated with the STING inhibitor H151 ($n = 5$/condition). Data are representative of at least three independent experiments with similar results. **F,** ID8-*Defb29/Vegfa* cells carrying control nontargeting sgRNA (sgCtrl), or devoid of IRF3 (sgIRF3), were exposed to deferiprone, and expression of the indicated genes was assessed by qRT-PCR ($n = 4$ per condition). Data are representative of five independent sgCtrl and sgIRF3 clones. **G–J,** Role of the DDR in deferiprone-induced MULT1 and DR5 on ovarian cancer cells. ID8-*Defb29/Vegfa* cells were pretreated for 1 hour with an ATR inhibitor (AZD6738, 1 µmol/L), ATM inhibitor (AZD0156, 100 nmol/L), or CHK1/2 inhibitor (AZD7762, 300 nmol/L). Then, deferiprone or vehicle was added, and expression of DR5 (**G** and **H**) and MULT1 (**I** and **J**) was analyzed by FACS 12 hours later ($n = 3$ technical replicates per condition). Experiments were repeated at least three independent times with similar results. Data are analyzed using violin plots with all data points (**B** and **C**); using bar plots with mean ± SEM (**D–F**, **H**, and **J**); with unpaired Student *t* test (**C** and **D**); using one-way ANOVA with Tukey multiple comparison test (**B**, **E**, and **F**); and using two-way ANOVA with Šídák's multiple comparisons test (**H–J**). BioRender.com

type-I IFN-NK cell axis in this setting. To confirm that type-I IFN specifically produced by deferiprone-exposed malignant cells mediated these effects, female mice were implanted with IRF3-deficient ovarian cancer cells (Supplementary Fig. S7F and S7G; Fig. 5F) and were then treated with the combination of cisplatin and deferiprone as described in Supplementary Fig. S8E. Of note, mice developing ID8-*Defb29/Vegfa* ovarian tumors lacking IRF3 in malignant cells demonstrated a significant reduction in NK cell infiltration after treatment compared with their IRF3-sufficient counterparts receiving the same therapy (Fig. 6E). These data highlight a central role for cancer cell-intrinsic IRF3/type-I IFN production in deferiprone-induced NK cell accumulation at metastatic ovarian cancer sites.

How does type-I IFN induced by deferiprone support antitumor NK cell responses? We sought to study the role of IL15 in the process as this cytokine promotes the survival, proliferation, and cytotoxicity of NK cells (47). Importantly, type-I IFN has been shown to induce expression of IL15 by DCs, which possess a remarkable capacity to "trans-present" this cytokine to neighboring NK cells (48–50). Indeed, we observed that bone marrow–derived DCs generated from IL15$^{2A\text{-}eGFP}$ reporter mice (51) strongly produced IL15 upon stimulation with recombinant IFNβ (Supplementary Fig. S8F). We thus examined whether enhanced type-I IFN production in the tumor microenvironment driven by deferiprone could induce IL15 expression by DCs residing in this milieu (20, 21, 24).

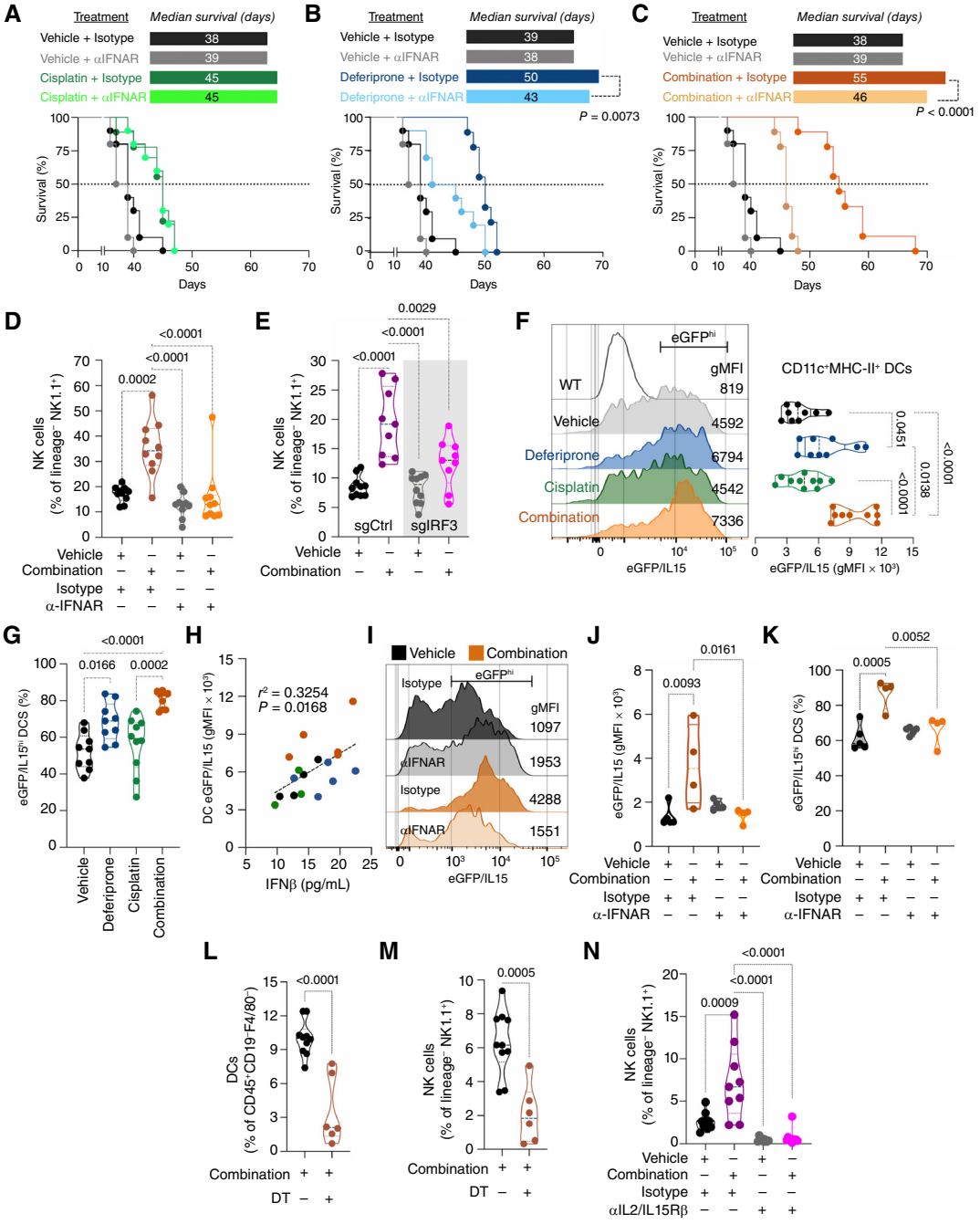

Figure 6. Deferiprone administration blunts ovarian cancer progression by inducing protective type-I IFN responses. **A–C,** Female mice developing metastatic ID8-*Defb29/Vegfa* tumors received IFNAR1-blocking or isotype control antibodies, as shown in Supplementary Fig. S8A, and Kaplan–Meier survival curves were generated for the indicated treatment groups ($n = 8$–10 mice/group). Median survival and exact *P* values for the log-rank (Mantel–Cox) test comparing groups treated with isotype or IFNAR1-blocking antibodies are shown. **D,** Female mice bearing advanced ID8-*Defb29/Vegfa* tumors were treated as indicated in Supplementary Fig. S8C, and NK cell proportions in the peritoneal cavity were analyzed thereafter ($n = 10$ mice/group). **E,** sgCtrl or sgIRF3 ID8-*Defb29/Vegfa* cells were implanted into female mice and treated as described in Supplementary Fig. S8E, and NK cell proportions in the peritoneal cavity were analyzed thereafter ($n = 9$–10 mice/group). **F–H,** IL15$^{2A\text{-}eGFP}$ female developing ID8-*Defb29/Vegfa* tumors were treated as described in Supplementary Fig. S8G ($n = 9$–10 mice/group). **F,** Representative histograms and violin plots of eGFP/IL15 expression in tDCs from peritoneal lavage samples. **G,** Percent of tDCs exhibiting high levels of IL15. **H,** Correlation between IFNβ concentration and eGFP/IL15 expression in tDCs ($n = 3$–5 mice/group). **I–K,** IL15$^{2A\text{-}eGFP}$ female mice bearing ID8-*Defb29/Vegfa* tumors were treated as described in Supplementary Fig. S8C. **I,** Representative histograms of eGFP/IL15 expression in tDCs from peritoneal lavage samples for the indicated groups. **J,** Violin plots showing the gMFI of eGFP/IL15 signal in tDCs of the indicated groups. **K,** Percent of tDCs exhibiting high levels of IL15 ($n = 4$–5 mice/group). **L** and **M,** *Itgax*-DTR-GFP female mice implanted with ID8-*Defb29/Vegfa* tumors were treated as described in Supplementary Fig. S8J. The proportion of (**L**) tDCs and (**M**) NK cells in the peritoneal cavity were analyzed by FACS ($n = 6$–10 mice/group). **N,** Female mice developing metastatic ID8-*Defb29/Vegfa* tumors were treated as shown in Supplementary Fig. S8N, and the percentage of NK cells was assessed by FACS. Data are analyzed using one-way ANOVA with Tukey multiple comparison test (**D–K** and **N**); with unpaired Student *t* test (**L** and **M**); using Pearson correlation coefficient (r^2) (**H**); and exact *P* value for all the significant comparisons. BioRender.com

IL15$^{2A\text{-}eGFP}$ reporter mice bearing peritoneal ID8-*Defb29/Vegfa* tumors were acutely treated with vehicle control, cisplatin, deferiprone, or the combination of both drugs (Supplementary Fig. S8G), and immunophenotyping analyses were conducted thereafter. As expected, acute treatment with deferiprone, alone or in combination with cisplatin, increased the proportion of NK cells at tumor sites, and the extent of NK cell infiltration correlated with the levels of IFNβ in the peritoneal cavity (Supplementary Fig. S8H and S8I). Notably, these effects were accompanied by a significant increase in the proportion of tumor-associated DCs (tDC) expressing high levels of IL15 compared with their control counterparts receiving vehicle or cisplatin alone (Fig. 6F and G). Enhanced IL15 expression by tDCs correlated with the abundance of IFNβ at tumor sites (Fig. 6H), and these responses were entirely abrogated upon antibody-mediated blockade of IFNAR1 (Fig. 6I–K). To functionally ascertain that DCs mediate NK cell infiltration in response to deferiprone, we used *Itgax*-DTR-GFP mice (52) that enable the depletion of CD11c$^+$ DCs upon diphtheria toxin (DT) administration. These transgenic mice were implanted with ID8-*Defb29/Vegfa* ovarian tumors and then treated acutely with the combination of cisplatin and deferiprone, in the presence or absence of DT (Supplementary Fig. S8J). We observed robust depletion of tDCs (Fig. 6L; Supplementary Fig. S8K) and confirmed that NK cells present at tumor locations did not express CD11c or GFP in these transgenic hosts (Supplementary Fig. S8L), thus precluding their direct elimination upon DT administration. Notably, tDC depletion caused a drastic reduction in NK cell infiltration at tumor sites in mice receiving the combination treatment (Fig. 6M; Supplementary Fig. S8M). Finally, we sought to establish the role of IL15 signaling in deferiprone-mediated NK cell accumulation at tumor sites. Mice bearing ID8-*Defb29/Vegfa* tumors were treated with a blocking antibody against CD122, the beta subunit of the IL2/IL15 receptor (IL2/IL15Rβ), followed by administration of vehicle or combination therapy with cisplatin and deferiprone (Supplementary Fig. S8N). Of note, suppressing IL15 signaling through this approach completely prevented NK cell accumulation at tumor sites in response to the combination treatment (Fig. 6N). Therefore, iron chelation therapy using deferiprone elicits innate type-I IFN signaling in the ovarian cancer microenvironment, enhancing IL15 expression by tDCs that sustain NK cell–mediated control of metastatic progression.

DISCUSSION

In this study, we provide experimental evidence indicating that disruption of iron metabolism in ovarian cancer cells using a clinically available iron chelator represents a major opportunity to induce innate immune responses capable of delaying metastatic disease progression and enhancing the effects of first-line chemotherapy.

Multiple analyses reported herein uncover the clinical relevance of iron dysregulation in human ovarian cancer. First, evaluation of scRNA-seq and bulk RNA-seq data from HGSOC specimens identified the enrichment of iron-related signatures specifically in epithelial ovarian cancer cells, which had significant prognostic value in women with this disease. Second, we found high concentrations of iron in ascites samples obtained from patients with ovarian cancer, which correlated with the intrinsic levels of previously reported tumorigenic factors. Third, we determined that iron-transporting and iron-capturing proteins are markedly enriched in this malignant fluid, indicating that iron is readily available for metastatic ovarian cancer cells that inhabit the peritoneal cavity.

In various cancer types, targeting the excessive utilization of iron has been explored through strategies aimed at inducing ferroptosis (53). However, this approach demands specific conditions, including a defective anti-oxidant machinery and increased lipid peroxidation within the cancer cell, which may limit its full translational potential (54). Conversely, iron chelation has been widely used in diseases characterized by abnormal iron accumulation (55). Various iron chelators have received FDA approval for clinical use (56). Importantly, deferiprone is the only one with intracellular chelation capabilities (57, 58) that can facilitate iron redistribution within the organism, hence avoiding negative side effects associated with excessive iron excretion (57).

The complex microenvironments engendered by late-stage ovarian tumors that disseminate throughout the peritoneal cavity play a pivotal role as mediators of chemoresistance and immunosuppression (59, 60). Our study unveils that deferiprone administration reshapes the landscape of immune cells infiltrating this complex metastatic milieu, inducing significant accumulation of NK cells in the peritoneal cavity and the omentum that partly mediate the therapeutic effects of this drug. Since dysfunctional NK cells devoid of cytotoxic capacity are commonly found in the ascites of patients with ovarian cancer (61, 62), our findings suggest that treatment with deferiprone might represent a new strategy to reactivate these cells at strategic tumor sites.

Previous studies demonstrated that deferiprone can mitigate the adverse effects of inflammatory processes caused by mitochondrial iron accumulation (58, 63). In the context of cancer, deferiprone has been linked to the induction of mitochondrial dysfunction leading to mitophagy and uncontrolled production of reactive oxygen species in malignant cells (31, 64). Nonetheless, whether iron chelation could elicit immune-modulatory mechanisms in cancer hosts has not been established. Our research addressed this major gap in knowledge by revealing that deferiprone triggers cancer cell–intrinsic innate immune signaling driven by mtDNA sensing in the cytosol and activation of the nuclear DDR. These parallel effects culminate in the production of type-I IFN and the upregulation of NK cell–activating molecules on ovarian cancer cells (Fig. 7—proposed model).

Type-I IFN exerts potent anticancer effects driven by the activation of both innate and adaptive immune responses (46). Importantly, we found that deferiprone bolstered IL15 expression in tDCs by enhancing type-I IFN production by cancer cells at tumor sites. Depleting these intratumoral DCs, or blocking IL15 signaling, compromised protective NK cell accumulation at tumor locations in response to deferiprone administration. Accordingly, blocking type-I IFN signaling drastically reduced the OS benefit conferred by combination treatment with deferiprone and cisplatin in mice with metastatic ovarian cancer. Whether type-I IFN produced by tumor-resident stromal cells, such as fibroblasts, contribute to the observed therapeutic effects of deferiprone administration warrants further investigation.

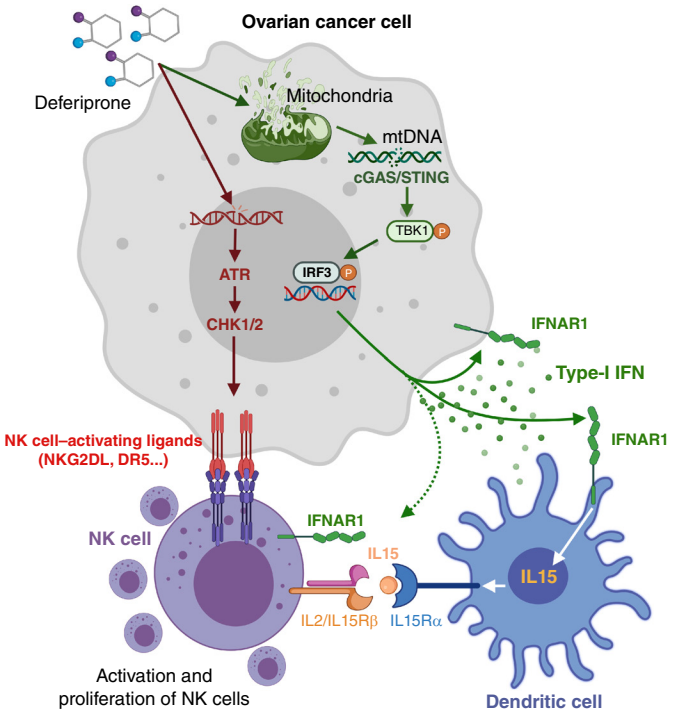

Figure 7. Proposed Model. Deferiprone exposure instigates two parallel innate immunostimulatory mechanisms in ovarian cancer cells; it triggers the DDR through ATR-CHK1/2 activation, bolstering surface expression of NK cell–activating molecules such as DR5 and MULT1. Concurrently, the drug disrupts mitochondrial integrity, leading to the release of mtDNA that induces type-I IFN via the cGAS-STING-IRF3 axis. Increased type-I IFN levels within the metastatic ovarian cancer microenvironment enhances IL15 expression by tDCs that promotes NK cell accumulation and function at tumor sites. (Created with BioRender.com.)

Taken together, our study reveals that iron chelation therapy with deferiprone evokes relevant effects against metastatic ovarian cancer by activating the type-I IFN-DC-NK cell axis (Fig. 7—proposed model). We propose that disrupting iron accumulation in the tumor microenvironment may represent a new immunotherapeutic approach for aggressive malignancies, like ovarian cancer, that are refractory to current T-cell–centric modalities such as immune checkpoint blockade and adoptive cellular therapy.

METHODS

Survival Analyses Using The Cancer Genome Atlas Patient Cohorts

The bulk RNA-sequencing (RNA-seq) expression data from The Cancer Genome Atlas (TCGA) was deconvoluted with PRISM (14) in order to separate signals from epithelial ovarian cancer cells (EOC), immune cells, and fibroblasts. Clinical data for TCGA cohort (13) were downloaded from cBioPortal database (http://www.cbioportal.org/study/summary?id=ov_tcga_pub). Analysis was carried out on R version 4.0.3. Using the Molecular Signatures Database (https://www.gsea-msigdb.org/), iron-related signatures were evaluated and those with significant *P* values were selected:

GO:0034755: GOBP_REGULATION_OF_IRON_ION_TRANSMEMBRANE_TRANSPORT; gene members: iron–sulfur cluster assembly enzyme (*ISCU*), homeostatic iron regulator (*HFE*), interferon gamma (*IFNG*), microRNA 210 (*MIR210*), ATPase copper-transporting alpha (*ATP7A*), beta-2-microglobulin (*B2M*), and transferrin (*TF*).

GO:0098711: GOBP_IRON_ION_IMPORT_ACROSS_PLASMA_MEMBRANE; gene members: iron–sulfur cluster assembly enzyme (*ISCU*), STEAP2 metalloreductase (*STEAP2*), interferon gamma (*IFNG*), microRNA 210 (*MIR210*), and solute carrier family 39 member 8 (*SLC39A8*).

GO:0008198: GOMF_FERROUS_IRON_BINDING; gene members: cysteine dioxygenase type 1 (*CDO1*), egl9 family hypoxia inducible factor 2 (*EGLN2*), egl9 family hypoxia inducible factor 3 (*EGLN3*), DnaJ heat shock protein family (*Hsp40*) member C24 (*DNAJC24*), alkB homolog 2, alpha-ketoglutarate–dependent dioxygenase (*ALKBH2*), alkB homolog 3, alpha-ketoglutarate–dependent dioxygenase (*ALKBH3*), ferrochelatase (*FECH*), iron–sulfur cluster assembly enzyme (*ISCU*), 3-hydroxyanthranilate 3,4-dioxygenase (*HAAO*), frataxin (FXN), ferritin heavy chain 1(*FTH1*), ferritin light chain (*FTL*), diphthamide biosynthesis 3 (*DPH3*), ferritin heavy chain 1 pseudogene 19 (*FTH1P19*), phytanoyl-CoA 2-hydroxylase (*PHYH*), ferritin heavy chain–like 17 (*FTHL17*), acid phosphatase 5, tartrate resistant (*ACP5*), egl9 family hypoxia inducible factor 1 (*EGLN1*), tet methylcytosine dioxygenase 2 (*TET2*), hypoxia inducible factor 1 subunit alpha inhibitor (*HIF1AN*), synuclein alpha (*SNCA*), transferrin (*TF*), tyrosine hydroxylase (*TH*), FTO alpha-ketoglutarate–dependent dioxygenase (*FTO*), alkB homolog 1, histone H2A dioxygenase (*ALKBH1*), ferritin mitochondrial (*FTMT*), and hephaestin (*HEPH*).

Signature expression scores for each deconvoluted cell type in each sample were calculated with AUCell version 1.12.0 (65), which calculates the activity of a gene set using a rank-based method. Six genes (*FTH1P19*, *MIR210*, *BOLA2B*, *ERFE*, *UQCRFS1P1*, and *CYP2G1P*) present in the studied iron-related signatures were not found in the bulk RNA-seq expression data. Gene set objects in R were created with the R package GSEABase version 1.52.1. Samples were generally divided into high and low signature score groups with the cutoffs set according to score tertiles: lowest tertile was annotated as "Low" and highest tertile was annotated as "High". For the signatures "GOBP_REGULATION_OF_IRON_ION_TRANSMEMBRANE_TRANSPORT" and "GOBP_IRON_ION_IMPORT_ACROSS_PLASMA_MEMBRANE", the scores in EOCs and fibroblasts were very low. Therefore, "Positive" samples were classified as samples with a nonzero score, whereas "Negative" samples were classified as samples with a score of 0.

Survival analysis was done using Cox proportional hazards model from the R package *survival* version 3.2-10. Proportional hazards assumptions of the Cox regression were tested with cox.zph function. Kaplan–Meier curves were plotted for visualization purposes using

R package *survminer* version 0.4.9. *P* values for survival analyses were adjusted using the p.adjust function from base R Stats Package with method set to "fdr".

Biological Specimens Derived from Patients with Ovarian Cancer

Plasma samples from cancer-free women were obtained from the New York Blood Center. Ascites samples from patients with stages III–IV HGSOC were obtained under written informed consent following appropriate biospecimen collection and use protocols were established at Weill Cornell Medicine (WCM) and Memorial Sloan Kettering Cancer Center. All human specimens were deidentified for subsequent experimental analyses. The ascites was centrifuged at 4°C for 10 minutes at 400 rcf, with subsequent separation of supernatants from cell pellets and filtration through 0.22-μm filters to eliminate cellular debris. The processed samples were cryopreserved at −80°C in small aliquots to minimize freeze–thaw cycles. Human samples' information is described in Supplementary Table S1.

Human Ovarian Cancer Cell Lines

SKOV3 and OVCAR3 cells were kindly provided by Dr. J. Conejo-Garcia. TYK-nu were purchased from the Japanese Collection of Research Bioresources Cell Bank (JCRB0234.0). All cell lines were tested for mycoplasma contamination.

Mice and Experimental Murine Ovarian Cancer Models

Female mice were housed in pathogen-free microisolator cages at the animal facilities of WCM and used at 8 to 12 weeks of age. All mouse experiments were approved by the Institutional Animal Care and Use Committee under protocol # 2011-0098. Wild-type (WT) C57BL/6J, B6.Cg-Rag2$^{tm1.1Cgn/J}$, and B6.FVB-1700016L21Rik$^{Tg(Itgax-HBEGF/EGFP)57Lan}$/J (Itgax-DTR) were purchased from The Jackson Laboratory. IL15 translational reporter mice (IL15$^{2A\text{-}eGFP}$) were kindly provided by Dr. Ross Kedl (Department of Immunology & Microbiology, University of Colorado Anschutz School of Medicine, Aurora, CO 80045) (66). Parental ID8 cells and the aggressive ID8-*Defb29/Vegfa* derivate were cultured and used as previously described (20, 67). Both cell lines were obtained under the Material Transfer Agreement (MTA) from Drs. K. Roby (University of Kansas Medical Center, Kansas City, KS) and J. Conejo-Garcia (Department of Integrative Immunobiology, Duke University School of Medicine, Durham, NC), respectively. The PPNM cell line (*Trp53*$^{-/-R172H}$*Pten*$^{-/-}$*Nf1*$^{-/-}$*Myc*^{OE}) was generously provided by Dr. R. Weinberg (Whitehead Institute for Biomedical Research, Cambridge, MA) under MTA (25). The MP cell line was generated as described previously (68). For tumor implantation, 1.5 × 10^6 ID8-based ovarian cancer cells suspended in 200 μL of sterile PBS were intraperitoneally injected into mice. Alternatively, PPNM cells were suspended in PBS containing Matrigel (Corning Matrigel Matrix, Cat# 47743-716) at 1:1 ratio, and 200 μL of the mix containing 1.0 × 10^6 cells was administered intraperitoneally` into WT mice, as reported previously (25). Metastatic progression, ascites accumulation, and host survival were monitored over time. Tumor burden in the peritoneal cavity was assessed by live bioluminescent imaging. Briefly, PPNM-bearing mice were given a single i.p. injection of VivoGlo Luciferin (2 mg/mouse; Promega, Cat# P1042) and then imaged on a Xenogen IVIS Spectrum *in vivo* imaging system at the Weill Cornell Research Animal Resource Center. All cell lines were verified for mycoplasma contamination and maintained under prophylactic Plasmocin supplementation (InvivoGen, Cat# ant-mpt).

Nucleic Acid Extraction and qPCR Analyses

Mouse or human total RNA was isolated using the RNeasy Mini kit (QIAGEN, Cat# 74106) or QIAzol lysis reagent (QIAGEN, Cat# 79306) according to the manufacturer's instructions. 0.1 to 1 μg of RNA was reverse transcribed to generate cDNA using the qScript cDNA Synthesis Kit (Quantabio, Cat# 95047). qRT-PCR was performed using PerfeCTa SYBR Green FastMix (Quantabio, Cat# 95071) on a QuantStudio 6 Flex qRT-PCR system (Applied Biosystems). Normalized gene expression was calculated by the comparative threshold cycle method using *ACTB* for human or *Actb* for mouse as endogenous controls. For cytosolic and mitochondrial DNA extraction, mitochondria were first obtained using the Mitochondria Isolation Kit for Cultured Cells (Thermo Fisher Scientific, Cat# 89874) according to the manufacturer's instructions. Then, DNA from cytosolic and mitochondrial fractions were extracted using the DNeasy Blood & Tissue Kit (QIAGEN, Cat# 69504) according to the manufacturer's instructions. Levels of *mt-Cox1* was compared with that of genomic *18S*. All primers used in this study are described in Supplementary Table S5.

Mouse RNA-seq

ID8-*Defb29/Vegfa* cells were treated with vehicle or deferiprone (Sigma-Aldrich, Cat# 379409) for 12 hours, and total RNA was subsequently isolated using the RNeasy MinElute kit (QIAGEN, Cat# 74204) according to the manufacturer's instructions. Quality control checks were conducted on all samples using an Agilent 2100 Bioanalyzer to ensure RNA integrity.

mRNA libraries were generated and sequenced at the Weill Cornell Genomics Resources core facility. Raw sequencing data underwent preprocessing and analysis using the Partek software, following a standard pipeline. RNA-seq data were aligned to the mm10 genome using GSNAP method, and Partek E/M was used to estimate read counts at the gene level, leveraging ensemble transcriptome information. To assess differential gene expression between experimental groups, a Gene Set Analysis method was applied. Gene expression changes were considered statistically significant if they met the FDR threshold of less than 5%. Additionally, gene set enrichment analysis was performed using Ingenuity Pathway Analysis (IPA, QIAGEN) with a focus on "Upstream regulators." Regulators with a statistical significance level (*P* value) lower than 10^{-6} and with predicted activation or inhibition states (*Z*-score > 2) were reported. This analysis identified key molecular regulators associated with the observed gene expression changes induced by the experimental treatments. RNA-seq data were deposited under NCBI Gene Expression Omnibus (GEO) Accession number (GSE246051).

Single-Cell RNA-seq

Human. For the analysis of single-cell RNA-seq (scRNA-seq) data, preprocessed counts from 22 HGSOC tumor specimens (11) were downloaded from GEO with accession code GSE165897. Individual cell scores for each signature were obtained using Ucell (v1.3.1; ref. 69), and a pairwise Wilcoxon test was performed to compare the average scores between fibroblasts, immune cells, and EOCs in each sample. scRNA-seq data from eight normal fallopian tube samples (12) were downloaded from CELL×GENE portal. Individual cell scores for each signature were obtained using Ucell (v1.3.1; ref. 69), and a Wilcoxon test was performed to compare the average scores between EOCs and secretory cells. At the same time, to avoid detecting significant differences due only to batch effect, Wilcoxon tests were calculated between the mean signature score of the secretory cells of each sample and the fibroblasts and immune cells of the same normal samples.

Mouse. The cellular fraction of peritoneal lavage samples was isolated from mice bearing ID8-*Defb29/Vegfa* ovarian cancer for 35 days and subjected to scRNA-seq. Library preparation, sequencing, and raw data preprocessing were performed at the WCM Epigenomics Core Facility using the Illumina HiSeq 2500 platform. Subsequently, the reads underwent processing and analysis utilizing Seurat

4.1.2 (70). After subsetting low-quality data (min. cells = 3, min. features = 200, nFeature_RNA min = 200 max = 2,500, percent.mt < 5), 6,502 cells were obtained and log-normalized. Nonlinear dimensional reduction using Uniform Manifold Approximation and Projection (UMAP) with default parameters (dims = 1:10, n_neighbors = 30, metric = cosine, n_trees = 50) was used to obtain cell clusters. The top 10 significant clusters' markers were found (FindAllMarkers min.pct = 0 logfc.threshold = 0) to corroborate cell types. Lineage putative genes were used to identify the immune cell, and the tumor cell clusters were designed according to the differentially expressed genes using IPA (QIAGEN) for the top cell function based on the following predetermined categories—invasive: cellular movement category [P value = 1.05×10^{-23}, z-score 2.81 (92 members upregulated)], proliferative: cell cycle category [P value = 1.24×10^{-14}, z-score 2.23 (39 members upregulated)], Stem-like: embryonic development category [P value = 5.76×10^{-12}, z-score 1.87 (63 members upregulated)], also the expression of putative cancer stem cell genes was evaluated: glutathione S-transferase mu 2 (*Gstm2*, P value 2.8×10^{-297}, avg_Log (FC) = 1.22), aldehyde dehydrogenase 1 family member A1 [*Aldh1a*, P value: 6.5×10^{-179}, avg_Log (FC) = 0.68], SRY-box transcription factor 9 [*Sox9*, P value: 3.63×10^{-137}, avg_Log (FC) = 0.62], SRY-box transcription factor 4 [*Sox4*, P value: 4.94×10^{-70}, avg_Log (FC) = 0.38], and Chemo-resistant: embryonic development category P value = 2.70×10^{-22}, z-score 1.61 (68 members upregulated); this cluster also exhibited high expression of the multidrug resistance ATP binding cassette subfamily B member 1 [*Abcb1b*, P value: 1.20×10^{-257}, avg_Log (FC) = 0.68].

Gene sets related to iron metabolism were obtained from the Molecular Signatures Database v7.5.1 for *Mus musculus* in the ontology gene sets (C5), and signatures related to disease were excluded. Single-sample Gene Set Enrichment Analysis was used to calculate enrichment scores for iron-related gene sets. These scores were then obtained using Escape v.1.20 (using the function enrichIt) and plotted for each cell type. Mouse scRNA-seq data were deposited under NCBI GEO Accession number (GSE246051).

Cytokine and Chemokine Quantification

Human undiluted ascites samples were submitted to Eve Technologies Assay Services for analysis using the Human Cytokine/Chemokine 71-Plex Discovery Assay Array. To obtain peritoneal lavage samples from tumor-bearing mice, we injected 5 mL of sterile PBS, and the liquid was aspirated using a 10-mL syringe with a 20 G1 1/2 needle. During collection, the needle was detached to avoid mechanical red blood cells lysis. Subsequently, the samples were concentrated utilizing 3 K Amicon tubes (Millipore, Cat# UFC800324), and all samples were normalized to a final protein concentration of 5 mg/mL. Mouse samples were submitted to Eve Technologies Assay Services for analysis using the Mouse Cytokine/Chemokine 44-Plex Discovery Assay Array.

Ovarian Cancer Organoid Development, Characterization, and Maintenance

Patient-derived fresh tissue samples were collected with written informed patient consent with the approval of the Institutional Review Board (#1305013903) at WCM. Patient-derived tumor organoid lines were developed as described (71) with some modifications. Briefly, fresh tissue samples were washed three times with transport media [DMEM (Gibco, Cat# 11971025) with 1× GlutaMAX (Invitrogen, Cat# 35050079), 100 U/mL penicillin, 100 μg/mL streptomycin (Gibco, Cat# 15140148), Primocin 100 μg/mL (InvivoGen, Cat# ant-pm), and 10 μmol/L Rock inhibitor Y-27632 (Selleck Chemical Inc., Cat# S1049)] and placed in a sterile 3-cm petri dish (Falcon) for mechanical dissection into smaller pieces (~2 mm diameter) prior to enzymatic digestion. Enzymatic digestion was done with collagenase media [DMEM (Gibco, Cat# 11971025, 100 U/mL penicillin, 100 μg/mL streptomycin (Gibco, Cat# 15140148), 250 U/mL collagenase IV (Life Technologies, Cat# 17104019), 100 μg/mL Primocin (InvivoGen, Cat# ant-pm), and 10 μmol/L Rock inhibitor Y-27632 (Selleck Chemical Inc., Cat# S1049)] in a volume of at least 20 times the tissue volume and incubated on a shaker at 200 rpm at 37°C until the digestion solution turned cloudy, typically 30 to 45 minutes. The suspension was centrifuged at 300 rcf for 3 minutes, and the cell pellet was washed once with washing media [Advanced DMEM (Gibco, Cat# 12491023), 100 U/mL penicillin, 100 μg/mL streptomycin (Gibco, Cat# 15140148), 1× GlutaMAX (Cat# 35050079), and 1× HEPES (Invitrogen, Cat# 5630130)]. The cells were resuspended in a small volume of tissue type–specific primary culture media: Advanced DMEM (Gibco, Cat# 12491023) with 1× GlutaMAX (Cat# 35050079), HEPES (Invitrogen, Cat# 5630130), B27 (Gibco, Cat# A1486701), 100 U/mL penicillin, 100 μg/mL streptomycin (Gibco, Cat# 15140148), 100 μg/mL Primocin (InvivoGen, Cat# ant-pm), 10% Noggin conditioned media, 10% R-Spondin conditioned media, 10 mmol/L nicotinamide (Sigma-Aldrich, Cat# 72340), 1.25 mmol/L N-acetylcysteine (Sigma-Aldrich, Cat# A0737), 1 ng/mL Recombinant Human FGF-b (PeproTech, Cat# 100-18B), 20 ng/mL Recombinant Human FGF10 (PeproTech, Cat# 100-26), 1 μmol/L PGE2 (R&D Systems, Cat# 2296), 10 μmol/L SB202190 (Sigma-Aldrich, Cat# S7067), 50 ng/mL Mouse Recombinant EGF (Invitrogen, Cat# 315-09), 10 μmol/L Y-27632 (Selleck Chemical Inc., Cat# S1049), 10 ng/mL Heregulin beta1 (PeproTech, Cat# 100-03), 500 nmol/L A-83-01 (Tocris Bioscience, Cat# 2939), and 100 μmol/L β-Estradiol (Sigma-Aldrich, Cat# E8875). Up to ten 100 μL drops of Matrigel/cell suspension were distributed into a six-well cell suspension culture plate. The drops were allowed to polymerize for 30 minutes inside the incubator at 37°C and 5% CO_2 and afterward, 3-mL tumor type–specific primary culture media were added per well. Fresh culture media were replaced every 3 to 4 days. Patient-derived tumor organoids at approximately 300 to 500 μm were passaged using TrypLE Express (Gibco, Cat# 12604013) for 10 minutes in the water bath at 37°C. Single cells and small cell clusters were replated according to the procedure described above. Monthly mycoplasma screening was performed using the PCR Mycoplasma Detection Kit (abm, Cat# G238).

Treatment of Ovarian Cancer Organoids with Deferiprone

Fifty thousand cells obtained from disaggregated organoids were plated in a 100-μL cell culture media and Matrigel mix (v/v 2:1) in six-well plates. Three domes were plated in each well of a six-well plate. Plates were incubated for 30 minutes at 37°C to allow polymerization of the drops, and then 3 mL of tissue-specific primary culture media described above was added to each well. After 72 hours of plating, the media were aspirated, replaced with 3 mL PBS, and incubated for 10 minutes. This PBS wash was repeated one more time, and then 0, 100, 150, or 200 μmol/L deferiprone (Sigma-Aldrich, Cat# 379409) was added in 3 mL of fresh media made without B27. After incubation for 96 hours, cells were dissociated as described above and collected for downstream analysis.

In vitro Drug Treatments

Ovarian cancer cell lines were seeded and allowed to attach overnight. Subsequently, deferiprone (Sigma-Aldrich, Cat# 379409) or aphidicolin (Sigma-Aldrich, Cat# A0781) were added at a 2× concentration in fresh medium and incubated for specified time intervals. After the incubation periods, cells were rinsed with PBS and then detached for downstream analysis. For treatment with inhibitors H-151 (1 μmol/L, InvivoGen, Cat# inh-h151), Ataxia Telangiectasia and Rad3–related (ATR) inhibitor (1 μmol/L, AZD6738, Selleckchem, Cat# S7693), Ataxia Telangiectasia–Mutated (ATM) inhibitor (100 nmol/L, AZD0156, Selleckchem, Cat# S8375), CHK1/2 inhibitor (300 nmol/L, AZD7762, Selleckchem, Cat# S1532), cells were preincubated for

2 hours before treatment with deferiprone or aphidicolin. For all the experiments, working solutions of deferiprone were freshly prepared in culture medium at a concentration of 10 mmol/L, followed by the preparation of dilutions at the specified concentrations in culture medium.

Thiazolyl Blue Tetrazolium Bromide Assay for Cytotoxicity and Synergy

Ovarian cancer cells were seeded at a density of 3×10^3 cells per well in 96-well plates containing 100 μL of culture medium. These plates were then incubated overnight at 37°C with 5% CO_2. On the following day, 100 μL of deferiprone (2× concentration) was added and incubated for the specified time points. After the treatment, the cells were rinsed with RPMI medium without phenol red. Then, 100 μL of RPMI without phenol red and 50 μL of 1 mg/mL Thiazolyl Blue Tetrazolium Bromide (MTT) in sterile water were added to each well. The cells were incubated for 2 hours, followed by centrifugation, and washed with cold PBS. The plates were dried, and 100 μL of DMSO was added. After incubating for 30 minutes with shaking, the absorbance was measured at 540 nm using a SpectraMax iD3 instrument (Molecular Devices). For *in vitro* synergy analysis, serial dilutions of cisplatin (Sigma-Aldrich, Cat# 479306) and deferiprone (Sigma-Aldrich, Cat# 379409) were prepared and mixed to the desired concentrations and incubated for 48 hours, then MTT was performed to calculate the percentage of viability, and the Bliss synergy scores were calculated using synergy finder 3.0 (72).

Seahorse Analyses

ID8-*Defb29/Vegf-A* were plated at a density of 2.5×10^5 cells per well overnight; next day, the cells were treated with vehicle or deferiprone (Sigma-Aldrich, Cat# 379409) at 100 or 200 μmol/L for 6 hours; then, the cells were washed and nonbuffered XF Base Medium (Agilent, Cat# 102353-100) containing 25 mmol/L glucose (Sigma-Aldrich, Cat# G7021), 2 mmol/L L-glutamine (Gibco, Cat# 25030081), and 1 mmol/L sodium pyruvate (Gibco, Cat# 11360070) at pH = 7.4 was added. Cells were plated and oxygen consumption rate (OCR) measurements were analyzed on an XFe96 Extracellular Flux Analyzer (Agilent). After, basal OCR measurements were obtained, an OCR trace was recorded in response to oligomycin (1 μmol/L), carbonyl cyanide-p-(trifluoromethoxy) phenylhydrazone (FCCP, 1 μmol/L), and rotenone and antimycin (0.5 μmol/L each) following the XF Cell Mito Stress test kit (Agilent, Cat# 103010-100). After analysis, the cell numbers of each well were determined by nuclear DNA staining with Hoechst 33342 (Sigma-Aldrich, Cat# H3570) and OCR values were normalized accordingly. Finally, metabolic parameters were calculated using the seahorse Agilent Wave software (Agilent). At least 10 technical replicates per treatment were examined.

Generation of IRF3-Deficient Ovarian Cancer Cell Lines Using CRISPR/Cas9

Twenty-nucleotide sgRNAs directed against murine *Irf3* (NM_016849.4) were designed to target the genomic sequences CCAGTGGTGCCTACACC**CCG** (IRF3 sgRNA#1) and TGAACCGGAAAGAAGTGTTG (IRF3 sgRNA#2) (the three additional nucleotides highlighted in bold represent the protospacer adjacent motif). These target sequences correspond to exon 3 of the murine *Irf3* cDNA and were chosen using the Broad Institute's CRISPick tool (https://portals.broadinstitute.org/gppx/crispick/public). As a control, a scrambled sgRNA (sgCtrl) was used harboring a 20-nucleotide sequence that is computationally designed to be nontargeting within the murine genome. The RNA sequence for this nontargeting control was CGUUAAUCGCGUAUAAUACG. To generate Irf3-deficient ovarian cancer lines, *ID8-Defb29/Vegf-A* were electroporated with ATTO550-labeled sgRNA-Cas9 complexes using the Neon transfection system, according to the manufacturer's protocol [Integrated DNA Technologies (IDT), Cat# 1075931]. All materials for sgRNA-Cas9 complex generation were purchased from IDT and prepared as instructed in the IDT protocols using Neon transfection system. Cells were electroporated with either scrambled sgRNA-Cas9 complexes or the two *Irf3* sgRNA-Cas9 complexes with sequences described above. Twenty-four hours after electroporation, fluorescently labeled ATTO550$^+$ single cells for each condition were sorted by FACS, expanded, and screened for *Irf3* ablation separately. To screen for IRF3 ablation, Western blot analysis using rabbit anti-mouse IRF3 (Cell Signaling Technology, Cat# D83B9) was performed on total protein isolated from cells electroporated with sgRNA-Cas9 complexes containing the *Irf3* sgRNA-Cas9 described above. Following knockout confirmation in 16 clones from the sgRNA#1 and 16 clones from the sgRNA#2, random clones from the IRF3 sgRNA#2 and sgCtrl were used for deferiprone experiments. For *in vivo* experiments, three randomly selected sgCtrl and sgIRF3 clones with no growth defects were used. These clones were growth separately and admixed in equal parts prior to i.p. implantation.

Iron Quantification

For total iron measurements, 50 μL of ascites fluid was digested in 50 μL 50% HNO_3 water with 0.1% digitonin. Digested ascites samples were subsequently diluted 1:50 in 0.2% HNO_3 water and 20 μL of sample or iron standard measured by graphite furnace atomic absorption spectroscopy. For heme iron measurements, a method based on the conversion of the heme moiety to its fluorescent porphyrin derivative by the removal of heme iron under acidic reducing conditions was used (73, 74). Then, 200 μL of ascites fluid was centrifuged at 1,000 rfc for 5 minutes to remove cellular debris. Ascites supernatants were divided into two 100 μL aliquots and 500 μL, 2 mol/L oxalic acid added to each. One aliquot was heated to 95°C for 30 minutes to release iron from heme and generate fluorescent protoporphyrin IX. The other aliquot was left at room temperature for 30 minutes. Both aliquots were centrifuged for 10 minutes at 1,000 rfc at 4°C to remove debris. Then, 200 μL of the heated and unheated aliquots were placed into a black 96-well clear-bottomed cell culture microplate (Greiner Bio-One, Cat# 655090, Lot: E19083A9) and the fluorescence read at ex404 nm/em630 nm. The background fluorescence of the unheated aliquot was subtracted from the heated aliquot, and the extinction coefficient of heme at 630 nm (1 μmol/L heme = 15,200 fluorescence units) was used to determine heme concentrations as previously described (74).

Assessment of Total Reducing Iron and M-Aconitase Activity

About 1.5×10^6 ID8-*Defb29/Vegf-A* ovarian cancer cells suspended in 200 μL of sterile PBS was intraperitoneally injected into mice. Twenty-nine days later, one dose of deferiprone (150 mg/kg) or saline were injected intraperitoneally, and 8 hours later, the peritoneal lavage was recovered as described before. Single-cell suspensions were obtained, and tumor cells were sorted using a Sony MA900 (Sony) at the WCM CLC Flow Cytometry Core Facility. Sorted tumor cells were analyzed for total reducing iron using FerroOrange, and mitochondrial aconitase (m-aconitase) activity was measured simultaneously. FerroOrange was purchased form Dojindo Laboratories (F374) and used according to manufacturer protocols. Briefly, 0.2×10^6 sorted cells were incubated with 1 μmol/L FerroOrange solution and incubated for 30 minutes and viable cells were then analyzed by FACS. Then, m-aconitase activity was measured using the Aconitase Assay Kit from Abcam (ab83459), following the manufacturer instructions. Briefly, 0.5×10^6 sorted tumor cells were centrifuged and washed with sterile PBS. The supernatant was removed, and the cell pellet was stored at −80°C until analysis.

Proteomic Analyses

Ascites samples were separated using SDS-PAGE and stained with Simplyblue Safestain (Thermo Fisher Scientific, Cat# LC6065), eight bands were identified and cut. Individual bands were submitted to the Weill Cornell Proteomics & Metabolomics Core Facility. Proteins were then concentrated by centrifugation and buffer exchange using the Amicon Ultra-0.5 centrifugal filter unit with Ultracel-3 membrane (Millipore, Cat# UFC5003), in accordance with the manufacturer's protocol, with the exchange buffer consisting of 4 mol/L urea, 1 mol/L thiourea, and 50 mmol/L TEAB at pH 8.5. Proteins were reduced with 10 mmol/L dithiothreitol, incubated at 34°C for 1 hour, then alkylated with 58 mmol/L iodoacetamide for 45 minutes in dark at room temperature, and then quenched by a final addition of 36 mmol/L dithiothreitol. The solutions were then diluted with 50 mmol/L ammonium bicarbonate (pH 8.0) to a final buffer concentration of 1 mmol/L urea before trypsin digestion. Each sample was digested with 0.8 μg of trypsin for 18 hours at 37°C. The digestion was stopped by addition of TFA to a final pH of 2.2 to 2.5. The samples were then desalted with SOLA HRP SPE Cartridge (Thermo Fisher Scientific, Cat# 60109-001). First, the cartridges were conditioned with 1 × 0.5 mL 90% methanol and 0.1% TFA, and then equilibrated with 2 × 0.5 mL 0.1% TFA. The samples were diluted 1:1 with 0.2% TFA and were run slowly through cartridges. After washing with 2 × 0.5 mL of equilibration solution, peptides were eluted by 1 × 0.5 mL of 50% ACN and 0.1% TFA, and dried in a speed-vacuum centrifuge. Samples were reconstituted in 60 μL of 50% ACN and 0.1% TFA, and loaded onto columns right after the equilibration step, allowing slow flow-through. Cartridges were washed three times with 1.0 mL of equilibration solution and peptides were eluted two times with 0.6 mL of 50% ACN and 0.1% TFA, after which they were dried down in a speed-vacuum centrifuge for further use. The nano-LC–MS/MS analysis was carried out using UltiMate 3000 RSLCnano system (Dionex) coupled to an Orbitrap Fusion (Thermo Fisher Scientific) mass spectrometer equipped with a Nanospray Flex Ion Source. Each sample was reconstituted in 22 μL of 0.5% formic acid, and 10 μL was loaded onto an Acclaim PepMap 100 C18 trap column (5 μm, 100 μm × 20 mm, 100 Å, Thermo Fisher Scientific) with nanoViper Fittings at 20 μL/minute of 0.5% formic acid for online desalting. After 2 minutes, the valve switched to allow peptides to be separated on an Acclaim PepMap C18 nano column (3 μm, 75 μm × 25 cm, Thermo Fisher Scientific). Mobile phase A consisted of 2% ACN and 0.1% formic acid in water, and mobile phase B was 95% ACN and 0.1% formic acid in water, and the 120 minutes gradient was as follows: 5% to 23% to 35% B at 300 nL/minutes (3 to 83 to 123 minutes, respectively), followed by a 9-minute ramping to 90% B, a 9-minute hold at 90% B, and quick switch to 7% B in 1 minute. The column was re-equilibrated with 5% B for 20 minutes before the next run. A 10-fmol injection of standard BSA digest mixture with a short 30-minute gradient was run for quality control purposes. The Orbitrap Fusion instrument was operating in positive-ion mode with the nanospray voltage set at 1.7 kV and source temperature at 275°C. External calibration for Fourier transform, ion trap, and quadrupole mass analyzers was performed before the analysis. The Orbitrap full MS survey scan (m/z 400–1,800) was followed by the top 3-second, data-dependent higher collision dissociation (HCD) product–dependent electron-transfer dissociation (ETD) MS/MS scans for precursor peptides with 2 to 8 charges above a threshold ion count of 50,000 with normalized collision energy of 32%. Mass spectrometry survey scans were acquired at a resolving power of 120,000 (full-width-at-half-maximum at m/z 200), with automatic gain control (AGC) = 2×10^5, maximum injection time (maximum IT) = 50 ms, and HCD MS/MS scans at resolution 30,000 with AGC = 5 × 104, maximum IT = 60 ms, and with Q isolation window (m/z) at 3 for the mass range m/z 105 to 2,000. Dynamic exclusion parameters were set at 1 within 60-second exclusion duration with ± 10 parts per million exclusion-mass width. The product ion trigger list consisted of peaks at 204.0867 Da (HexNAc oxonium ion), 138.0545 Da (HexNAc fragment), 366.1396 Da (Hex-HexNAc oxonium ions), and 274.0927 Da (dehydrated N-acetylneuraminic acid). If one of the HCD product ions in the list was detected, two charge-dependent ETD MS/MS scans with HCD supplementary activation (for electron transfer and higher-energy collision dissociation scan) on the same precursor ion were triggered and collected in a linear ion trap. For doubly charged precursors, the ETD reaction time was set at 150 ms and the supplementary activation energy was set at 25%, and the same parameters set at 125 ms and 20%, respectively, were used for higher-charged precursors. For both ion-triggered scans, the fluoranthene ETD reagent target was set at 2×10^5, the AGC target at 1×10^4, maximum IT at 105 ms, and isolation window at 3. All data were acquired using Xcalibur 3.0 operation software and Orbitrap Fusion Tune Application v.2.1 (Thermo Fisher Scientific). All mass spectrometry and MS/MS raw spectra from each sample were searched using Byonics v.2.8.2 (Protein Metrics) using *Homo sapiens* protein database containing 133,840 sequences and downloaded from UniProt TrEMBL on January 4, 2016. The peptide search parameters were as follows: two missed cleavages for full trypsin digestion with fixed carbamidomethyl modification of cysteine, variable modifications of methionine oxidation, and deamidation on asparagine and glutamine residues. The peptide mass tolerance was 10 parts per million, and fragment mass tolerance values for HCD and the electron transfer and higher-energy collision dissociation spectra were 0.05 Da and 0.6 Da, respectively. The maximum number of common and rare modifications was both set at 2. Identified peptides were filtered for maximum 2% FDR or 50 hits to the reverse database. The total abundance was calculated as the sum of the intensity for each protein in all bands, and the percentage was calculated from the total intensity.

Flow Cytometry

Analyses were conducted using fluorochrome-conjugated antibodies purchased from BioLegend, unless stated otherwise. Cells were washed with PBS, Fc-gamma receptor–blocked using TruStain FcX (anti-mouse CD16/32, 93), and then stained for surface markers at 4°C in the dark for 30 minutes using the following antibodies: anti-CD45 (30-F11, 1:200), anti-CD3 (17A2, 1:200), anti-CD4 (RM4-5, 1:200), anti-CD8α (53-6.7, 1:200), anti-CD11c (N418, 1:200), anti-I-A/I-E (M5/114.15.2, 1:400; Tonbo Biosciences), anti-CD11b (M1/70, 1:200), anti-F4/80 (BM8, 1:200), anti-Ly6g (1A81 1:200), anti-Ly6c (HK1.4, 1:200), anti-NK1.1 (PK136, 1:200), anti-TER119 (TER119, 1:200), anti-CD19 (6D5, 1:200), anti-CD27 (LG.3A10, 1:200), anti-CD71 (CY1G4, 1:200), anti-ULBP1/MULT1 (237104; R&D Systems; 1:50), rat IgG2A Isotype Control (54447; R&D Systems), anti-CD262 (DR5, TRAIL-R2) (MD5-1, 1:200), and anti-IgG Isotype Control (HTK888). Cells were then washed and stained with DAPI (BioLegend) or LIVE/DEAD Fixable Near-IR Dead Cell Stain for live/dead discrimination (Invitrogen). Flow cytometry was performed on a LSRII or a LSRFortessa X-20 instruments (BD Biosciences). Cell populations were sorted from peritoneal lavage or ascites samples from ovarian cancer–bearing mice using a FACSAria sorter (BD Biosciences) or a Sony MA900 (Sony) at the WCM CLC Flow Cytometry Core Facility, and flow cytometry data were analyzed using FlowJo v.10 (TreeStar).

Immunohistochemistry

Omentum samples were collected from tumor-bearing mice and embedded in paraffin, then slides were generated in the Microscopy and Imaging Core Facility of WCM and stained for NKp46 in the Center of Comparative Medicine & Pathology–Laboratory of Comparative Pathology of the Memorial Sloan Kettering Cancer Center/WCM. Slides were scanned and processed in a Axioscan 7 instrument (ZEISS),

and the images were analyzed in Fiji (ImageJ). NKp46 stained area and total tissue area were calculated by using the color deconvolution function; NKp46 staining was expressed as the percentage of total tissue area; and the average of 3 to 5 fields per sample was reported.

Western Blotting

Cancer cells were washed twice in 1× cold PBS, and cell pellets were lysed using RIPA lysis and extraction buffer (Thermo Fisher Scientific, Cat# 89900), supplemented with a protease and phosphatase inhibitor tablet (Millipore, Cat# 11697498001 and Roche, Cat# 04906837001). Homogenates were centrifuged at 14,000 rpm for 30 minutes at 4°C, and the supernatants were collected. Protein concentrations were determined using a BCA Protein Assay Kit (Thermo Fisher Scientific, Cat# 23225). Equivalent amounts of protein were separated via SDS-PAGE and transferred onto polyvinylidene difluoride membranes following standard protocols. The following antibodies were used: anti-beta actin (Cell Signaling Technology, Cat# 8457), anti-pTBK1 (Cell Signaling Technology, Cat# 5483), anti-TBK1 (Cell Signaling Technology, Cat# 3504), anti-pIRE3 (Cell Signaling Technology, Cat# 4947), anti-IRF3 (Cell Signaling Technology, Cat# 4302), anti-Chk1 (Cell Signaling Technology, Cat# 2360), anti-phospho-Chk1 (Cell Signaling Technology, Cat# 2348), HRP-conjugated Beta Actin Monoclonal Antibody (Thermo Fisher Scientific, Cat# MA5-15739-HRP), and goat anti-rabbit secondary antibodies conjugated with HRP (Thermo Fisher Scientific, Cat# 32460). SuperSignal West Pico (Thermo Fisher Scientific, Cat# 34580) or FEMTO chemiluminescent substrates (Thermo Fisher Scientific, Cat# 34095) were used to image blots in an iBright CL1000 instrument (Thermo Fisher Scientific), and band intensity was measured using ImageJ Fiji.

In vivo Treatments

WT B6 or B6.Cg-Rag2tm1.1Cgn/J (Rag2) reporter mice were implanted via i.p. injection with 1.5×10^6 ID8-*Defb29/Vegfa*, or 1.0×10^6 PPNM ovarian cancer cells. After 7 days, mice were treated intraperitonially (or by oral gavage when specified) every day with 150 mg/kg of deferiprone (Sigma-Aldrich, Cat# 379409) and/or once per week with 5 mg/kg cisplatin (Accord, Cat# 16729-288-11) during a span of 4 weeks, both drugs were prepared in sterile human-grade saline and filtered. For the acute administration approach, WT C57BL6/J, IL15$^{2A\text{-}eGFP}$, or Itgax-DTR mice bearing ovarian cancer for 21 days were intraperitonially treated with one dose of cisplatin (5 mg/kg; Accord, Cat# 16729-288-11) and/or deferiprone (150 mg/kg; Sigma-Aldrich, Cat# 379409) every day for a span of 3 (Itgax-DTR) or 7 consecutive days (C57BL6/J and IL15$^{2A\text{-}eGFP}$). For *in vivo* blocking of type-I IFN signaling, two approaches were used: survival approach with mice bearing ID8-*Defb29/Vegfa* tumors were intraperitonially treated every 3 days with isotype control antibodies (Bio X Cell, Cat# BE0083) or anti-IFNAR blocking antibodies (Bio X Cell, Cat# BE0241) at 200 μg/mouse, starting 3 days after tumor implantation until the mice reach endpoint criteria. Simultaneously, the mice received cisplatin and/or deferiprone as mentioned above.

Acute Administration Approach with IFNAR Blockade. Mice bearing ID8-*Defb29/Vegfa* tumors for 18 days received a dose of isotype control antibodies (Bio X Cell, Cat# BE0083) or anti-IFNAR blocking antibodies (Bio X Cell, Cat# #BE0241) at 200 μg/mouse; at day 21, the mice were intraperitonially treated with one dose of cisplatin (5 mg/kg; Accord, Cat# 16729-288-11) and/or deferiprone (150 mg/kg; Sigma-Aldrich, Cat# 379409) every day for a span of 7 consecutive days.

Acute Administration Approach with CD122 Blockade. Mice bearing ID8-*Defb29/Vegfa* tumors for 17 days received a dose of isotype control antibodies (Bio X Cell, Cat# BE0090) or anti-IL2/IL15Rβ blocking antibodies (Bio X Cell, Cat# BE0298) at 200 μg/mouse; at day 21, the mice were intraperitonially treated with one dose of cisplatin (5 mg/kg; Accord, Cat# 16729-288-11) and/or deferiprone (150 mg/kg; Sigma-Aldrich, Cat# 379409) every day for a span of 7 consecutive days.

For both treatments, the mice were humanely sacrificed at day 30, and peritoneal lavage was performed to collect the infiltrating cells for downstream analysis.

For *in vivo* depletion of NK cells, mice were intraperitonially treated every 6 days with PK136 (Bio X Cell, Cat# BE0036) and mouse IgG2a isotype control (Bio X Cell, Cat# BE0085) at 200 μg/mouse, and starting 6 days after tumor implantation followed by treatment with cisplatin and deferiprone as mentioned above. Initial preliminary *in vivo* experiments were conducted using deferiprone provided by Apopharma Inc. under MTA. Subsequent therapeutic and mechanistic experiments were performed using deferiprone from Sigma-Aldrich (Cat# 379409).

Dietary Iron Experiments

Isocaloric-modified AIN-93G rodent diet (Research Diets) containing 3, 45, or 300 ppm of iron citrate was provided *ad libitum* 1 week prior to tumor challenge. Then, 3.0×10^6 ID8 parental cells were intraperitonially implanted into WT C57BL6/6J mice, and mouse weight and status were monitored weekly or daily, until endpoint when the animals were humanely euthanized.

Mitochondrial Iron Content

To assess mitochondrial iron content, we utilized Mito-FerroGreen (#M489, Dojindo Laboratories) following the manufacturer's guidelines. In brief, the cells were seeded overnight to allow attachment, were washed two times with Hank's Balanced Salt solution (HBSS), and were subsequently incubated with 5 μmol/L Mito-FerroGreen (200 μL), prepared in HBSS for 30 minutes at 37°C. The cells were washed two times with HBSS, 100 μmol/L deferiprone (200 μL) was added to the cells, and they were incubated for 30 minutes at 37°C in 5% CO_2 incubator. The cells were washed two times with HBSS and subsequently 100 μmol/L ammonium iron (II) sulfate (200 μL) was added to the cells, and they were incubated for 1 hour at 37°C in 5% CO_2 incubator. To visualize the cell nuclei, DAPI was used as a counterstain. After three HBSS washes, fluorescence was observed using a fluorescence microscope at the Microscopy and Imaging Core Facility of WCM. The fluorescence signal was quantified using ImageJ software.

Illustrations

Illustrations and schemes were created with BioRender.com under publication license.

Data Availability

Data generated in this study are available in the GEO database under the accession numbers GSE246051 for bulk RNA-seq and GSE246051 for scRNA-seq. Further information and requests for resources and reagents should be directed to and will be fulfilled by the lead contact, Dr. Juan R. Cubillos-Ruiz (jur2016@med.cornell.edu).

Statistical Analyses

All statistical analyses were performed using the GraphPad Prism software (version 10.0.3). Significance for pairwise correlation analyses was calculated using the Spearman or Pearson correlation coefficient (r or r^2). Comparisons between two groups were assessed using unpaired two-tailed Student *t* test. Multiple comparisons were assessed by one-way ANOVA including Tukey multiple comparisons test or two-way ANOVA with Šidák's multiple comparison test with

single pooled variance. Host survival rates were compared using the log-rank (Mantel–Cox) test. For violin plots, all data points, median, and quartiles are shown; for bar plots, data are presented as mean ± SEM. Unless otherwise stated, exact significant *P* values are shown, and nonsignificant values are omitted.

Authors' Disclosures

C. Salvagno reports other support from the Cancer Research Institute–Irvington Postdoctoral Fellowship Program and grants from the Ovarian Cancer Research Alliance during the conduct of the study. A. Emmanuelli reports grants from the NIH during the conduct of the study. D. Zamarin reports grants and personal fees from AstraZeneca and Xencor; personal fees from Gilead Sciences, Daiichi Sankyo, Memgen, Astellas, and BioInvent; and other support from ImmunOs, Calidi Biotherapeutics, and Accurius Therapeutics outside the submitted work, as well as a patent for Oncolytic NDV for cancer therapy issued (patent number US12042534). K. Holcomb reports personal fees from Johnson & Johnson and from Abbott Laboratories outside the submitted work, as well as grants from Fujirebio Diagnostics. L. Galluzzi reports grants and personal fees from Lytix, Promontory Therapeutics, Onxeo, and Noxopharm; personal fees from AstraZeneca, OmniSeq, Longevity Labs, Inzen, Luke Heller Tec Pr2 Foundation, Imvax, Boehringer Ingelheim, EduCom, and from AbbVie outside the submitted work, as well as other support from SOTIO and Ricerchiamo. A. Vähärautio reports grants from the Sigrid Jusélius Foundation, Cancer Foundation Finland, ERA PerMed JTC2020/Academy of Finland, and Foundation for the Finnish Cancer Institute during the conduct of the study. J.R. Cubillos-Ruiz reports grants from the NIH, U.S. Department of Defense, Cancer Research Institute, and American Association for Cancer Research during the conduct of the study; grants and other support from Vescor Therapeutics; personal fees from Emerald Bioventures, Immagene B.V.; and other support from Autoimmunity Biologic Solutions, Inc. outside the submitted work, as well as patents on the use immune modulators for cancer treatment (patent numbers WO WO2021034414A2, US10988461B2, US10450566B2, WO2018102655A1). No disclosures were reported by the other authors.

Acknowledgments

We thank the Scientific Computing Unit, the Flow Cytometry Core Facility, the Proteomics and Metabolomics Core Facility, and the Genomics Resources Core Facility at WCM for their excellent assistance with multiple analyses. We are especially grateful to Dr. F.J. Carmona for providing critical comments and suggestions on this article. This work was partly supported by NIH R01 NS114653, CA271619, and CA282072 (to J.R. Cubillos-Ruiz); NIH R01 CA271915 (to L. Galluzzi); NIH R01 CA249054 (to C.E. Mason); U.S. Department of Defense W81XWH2010191, W81XWH-16-1-0438, W81XWH-22-OCRP-IIRA, W81XWH2110478, and W81XWH2110357 (to J.R. Cubillos-Ruiz); U.S. Department of Defense BC180476P1 and BC210945 (to L. Galluzzi); NIH training grants T32 5T32AI134632-02 and F31CA257631 (to A. Emmanuelli); a Stand Up To Cancer Innovative Research Grant SU2C-AACR-IRG-03-16 (to J.R. Cubillos-Ruiz); a Stand Up To Cancer Phillip A. Sharp Innovation in Collaboration Award SU2C-AACR-PS-24 (to J.R. Cubillos-Ruiz); the Cancer Research Institute–Irvington Postdoctoral Fellowship Program (to C.-S. Chae and C. Salvagno); The 2022 AACR–Bristol Myers Squibb Immuno-oncology Research Fellowship 22-40-15-HWAN (to S.-M. Hwang); the Sigrid Jusélius Foundation (to A. Vähärautio and L. Suominen); the Cancer Foundation Finland (to A. Vähärautio and L. Suominen); ERA PerMed JTC2020 PARIS/Academy of Finland project 344697L (to A. Vähärautio); Foundation for the Finnish Cancer Institute–K. Albin Johansson Cancer Research Fellowship (to A. Vähärautio); European Union's Horizon 2020 research and innovation programme under the Marie Skłodowska-Curie grant agreement No 101067835 (to M.K. Frey); Ovarian Cancer Research Alliance (to C. Salvagno and D. Zamarin); National Cancer Center Korea NCC-19112605 (to M. Song); and National Research Foundation of Korea MSIT 2020R1C1C1010303 and RS-2023-00213292 (to M. Song). The indicated Stand Up To Cancer research grants are administered by the American Association for Cancer Research–AACR, the scientific partner of SU2C.

Note

Supplementary data for this article are available at Cancer Discovery Online (http://cancerdiscovery.aacrjournals.org/).

Received December 1, 2023; revised May 28, 2024; accepted July 1, 2024; published first July 17, 2024.

REFERENCES

1. Hentze MW, Muckenthaler MU, Galy B, Camaschella C. Two to tango: regulation of Mammalian iron metabolism. Cell 2010;142:24–38.
2. Crielaard BJ, Lammers T, Rivella S. Targeting iron metabolism in drug discovery and delivery. Nat Rev Drug Discov 2017;16:400–23.
3. Wang Y, Yu L, Ding J, Chen Y. Iron metabolism in cancer. Int J Mol Sci 2018;20:95.
4. Torti SV, Torti FM. Iron and cancer: more ore to be mined. Nat Rev Cancer 2013;13:342–55.
5. Torti SV, Manz DH, Paul BT, Blanchette-Farra N, Torti FM. Iron and cancer. Annu Rev Nutr 2018;38:97–125.
6. Matulonis UA, Sood AK, Fallowfield L, Howitt BE, Sehouli J, Karlan BY. Ovarian cancer. Nat Rev Dis Primers 2016;2:16061.
7. Fucikova J, Palova-Jelinkova L, Klapp V, Holicek P, Lanickova T, Kasikova L, et al. Immunological control of ovarian carcinoma by chemotherapy and targeted anticancer agents. Trends Cancer 2022;8:426–44.
8. Basuli D, Tesfay L, Deng Z, Paul B, Yamamoto Y, Ning G, et al. Iron addiction: a novel therapeutic target in ovarian cancer. Oncogene 2017;36:4089–99.
9. Rockfield S, Raffel J, Mehta R, Rehman N, Nanjundan M. Iron overload and altered iron metabolism in ovarian cancer. Biol Chem 2017;398:995–1007.
10. Hider RC, Hoffbrand AV. The role of deferiprone in iron chelation. N Engl J Med 2018;379:2140–50.
11. Zhang K, Erkan EP, Jamalzadeh S, Dai J, Andersson N, Kaipio K, et al. Longitudinal single-cell RNA-seq analysis reveals stress-promoted chemoresistance in metastatic ovarian cancer. Sci Adv 2022;8:eabm1831.
12. Lengyel E, Li Y, Weigert M, Zhu L, Eckart H, Javellana M, et al. A molecular atlas of the human postmenopausal fallopian tube and ovary from single-cell RNA and ATAC sequencing. Cell Rep 2022;41:111838.
13. Cancer Genome Atlas Research Network. Integrated genomic analyses of ovarian carcinoma. Nature 2011;474:609–15.
14. Häkkinen A, Zhang K, Alkodsi A, Andersson N, Erkan EP, Dai J, et al. PRISM: recovering cell-type-specific expression profiles from individual composite RNA-seq samples. Bioinformatics 2021;37:2882–8.
15. Ford CE, Werner B, Hacker NF, Warton K. The untapped potential of ascites in ovarian cancer research and treatment. Br J Cancer 2020;123:9–16.
16. Kipps E, Tan DSP, Kaye SB. Meeting the challenge of ascites in ovarian cancer: new avenues for therapy and research. Nat Rev Cancer 2013;13:273–82.
17. Peng Y, Kajiyama H, Yuan H, Nakamura K, Yoshihara M, Yokoi A, et al. PAI-1 secreted from metastatic ovarian cancer cells triggers the tumor-promoting role of the mesothelium in a feedback loop to accelerate peritoneal dissemination. Cancer Lett 2019;442:181–92.

18. Matei D, Kelich S, Cao L, Menning N, Emerson RE, Rao J, et al. PDGF BB induces VEGF secretion in ovarian cancer. Cancer Biol Ther 2007;6:1951–9.
19. Son D-S, Parl AK, Rice VM, Khabele D. Keratinocyte chemoattractant (KC)/human growth-regulated oncogene (GRO) chemokines and pro-inflammatory chemokine networks in mouse and human ovarian epithelial cancer cells. Cancer Biol Ther 2007;6:1308–12.
20. Conejo-Garcia JR, Benencia F, Courreges MC, Kang E, Mohamed-Hadley A, Buckanovich RJ, et al. Tumor-infiltrating dendritic cell precursors recruited by a beta-defensin contribute to vasculogenesis under the influence of Vegf-A. Nat Med 2004;10:950–8.
21. Cubillos-Ruiz JR, Silberman PC, Rutkowski MR, Chopra S, Perales-Puchalt A, Song M, et al. ER stress sensor XBP1 controls anti-tumor immunity by disrupting dendritic cell homeostasis. Cell 2015;161:1527–38.
22. Song M, Sandoval TA, Chae C-S, Chopra S, Tan C, Rutkowski MR, et al. IRE1α-XBP1 controls T cell function in ovarian cancer by regulating mitochondrial activity. Nature 2018;562:423–8.
23. Taher AT, Saliba AN. Iron overload in thalassemia: different organs at different rates. Hematology Am Soc Hematol Educ Program 2017;2017:265–71.
24. Chae C-S, Sandoval TA, Hwang S-M, Park ES, Giovanelli P, Awasthi D, et al. Tumor-derived lysophosphatidic acid blunts protective type I interferon responses in ovarian cancer. Cancer Discov 2022;12:1904–21.
25. Iyer S, Zhang S, Yucel S, Horn H, Smith SG, Reinhardt F, et al. Genetically defined syngeneic mouse models of ovarian cancer as tools for the discovery of combination immunotherapy. Cancer Discov 2021;11:384–407.
26. Papandreou I, Cairns RA, Fontana L, Lim AL, Denko NC. HIF-1 mediates adaptation to hypoxia by actively downregulating mitochondrial oxygen consumption. Cell Metab 2006;3:187–97.
27. Quirós PM, Prado MA, Zamboni N, D'Amico D, Williams RW, Finley D, et al. Multi-omics analysis identifies ATF4 as a key regulator of the mitochondrial stress response in mammals. J Cell Biol 2017;216:2027–45.
28. Vitale I, Pietrocola F, Guilbaud E, Aaronson SA, Abrams JM, Adam D, et al. Apoptotic cell death in disease—current understanding of the NCCD 2023. Cell Death Differ 2023;30:1097–154.
29. Muckenthaler MU, Rivella S, Hentze MW, Galy B. A red carpet for iron metabolism. Cell 2017;168:344–61.
30. Cardenas-Rodriguez M, Chatzi A, Tokatlidis K. Iron-sulfur clusters: from metals through mitochondria biogenesis to disease. J Biol Inorg Chem 2018;23:509–20.
31. Hara Y, Yanatori I, Tanaka A, Kishi F, Lemasters JJ, Nishina S, et al. Iron loss triggers mitophagy through induction of mitochondrial ferritin. EMBO Rep 2020;21:e50202.
32. Marchi S, Guilbaud E, Tait SWG, Yamazaki T, Galluzzi L. Mitochondrial control of inflammation. Nat Rev Immunol 2023;23:159–73.
33. West AP, Shadel GS. Mitochondrial DNA in innate immune responses and inflammatory pathology. Nat Rev Immunol 2017;17:363–75.
34. Decout A, Katz JD, Venkatraman S, Ablasser A. The cGAS–STING pathway as a therapeutic target in inflammatory diseases. Nat Rev Immunol 2021;21:548–69.
35. Petro TM. IFN regulatory factor 3 in health and disease. J Immunol 2020;205:1981–9.
36. Yamazaki T, Kirchmair A, Sato A, Buqué A, Rybstein M, Petroni G, et al. Mitochondrial DNA drives abscopal responses to radiation that are inhibited by autophagy. Nat Immunol 2020;21:1160–71.
37. Haag SM, Gulen MF, Reymond L, Gibelin A, Abrami L, Decout A, et al. Targeting STING with covalent small-molecule inhibitors. Nature 2018;559:269–73.
38. Ward DM, Cloonan SM. Mitochondrial iron in human health and disease. Annu Rev Physiol 2019;81:453–82.
39. Federico G, Carrillo F, Dapporto F, Chiariello M, Santoro M, Bellelli R, et al. NCOA4 links iron bioavailability to DNA metabolism. Cell Rep 2022;40:111207.
40. Maréchal A, Zou L. DNA damage sensing by the ATM and ATR kinases. Cold Spring Harb Perspect Biol 2013;5:a012716.
41. Klapp V, Álvarez-Abril B, Leuzzi G, Kroemer G, Ciccia A, Galluzzi L. The DNA damage response and inflammation in cancer. Cancer Discov 2023;13:1521–45.
42. Gasser S, Orsulic S, Brown EJ, Raulet DH. The DNA damage pathway regulates innate immune system ligands of the NKG2D receptor. Nature 2005;436:1186–90.
43. Baranovskiy AG, Babayeva ND, Suwa Y, Gu J, Pavlov YI, Tahirov TH. Structural basis for inhibition of DNA replication by aphidicolin. Nucleic Acids Res 2014;42:14013–21.
44. Mizutani T, Neugebauer N, Putz EM, Moritz N, Simma O, Zebedin-Brandl E, et al. Conditional IFNAR1 ablation reveals distinct requirements of Type I IFN signaling for NK cell maturation and tumor surveillance. Oncoimmunology 2012;1:1027–37.
45. Swann JB, Hayakawa Y, Zerafa N, Sheehan KC, Scott B, Schreiber RD, et al. Type I IFN contributes to NK cell homeostasis, activation, and antitumor function. J Immunol 2007;178:7540–9.
46. Zitvogel L, Galluzzi L, Kepp O, Smyth MJ, Kroemer G. Type I interferons in anticancer immunity. Nat Rev Immunol 2015;15:405–14.
47. Ma S, Caligiuri MA, Yu J. Harnessing IL-15 signaling to potentiate NK cell-mediated cancer immunotherapy. Trends Immunol 2022;43:833–47.
48. Mattei F, Schiavoni G, Belardelli F, Tough DF. IL-15 is expressed by dendritic cells in response to type I IFN, double-stranded RNA, or lipopolysaccharide and promotes dendritic cell activation. J Immunol 2001;167:1179–87.
49. Boudreau JE, Stephenson KB, Wang F, Ashkar AA, Mossman KL, Lenz LL, et al. IL-15 and type I interferon are required for activation of tumoricidal NK cells by virus-infected dendritic cells. Cancer Res 2011;71:2497–506.
50. Castillo EF, Stonier SW, Frasca L, Schluns KS. Dendritic cells support the in vivo development and maintenance of NK cells via IL-15 trans-presentation. J Immunol 2009;183:4948–56.
51. Kansler ER, Dadi S, Krishna C, Nixon BG, Stamatiades EG, Liu M, et al. Cytotoxic innate lymphoid cells sense cancer cell-expressed interleukin-15 to suppress human and murine malignancies. Nat Immunol 2022;23:904–15.
52. Jung S, Unutmaz D, Wong P, Sano G, De los Santos K, Sparwasser T, et al. *In vivo* depletion of $CD11c^+$ dendritic cells abrogates priming of $CD8^+$ T cells by exogenous cell-associated antigens. Immunity 2002;17:211–20.
53. Hassannia B, Vandenabeele P, Vanden Berghe T. Targeting ferroptosis to iron out cancer. Cancer Cell 2019;35:830–49.
54. Dixon SJ, Stockwell BR. The hallmarks of ferroptosis. Annu Rev Cancer Biol 2019;3:35–54.
55. Abbasi U, Abbina S, Gill A, Takuechi LE, Kizhakkedathu JN. Role of iron in the molecular pathogenesis of diseases and therapeutic opportunities. ACS Chem Biol 2021;16:945–72.
56. Richardson DR. The therapeutic potential of iron chelators. Expert Opin Investig Drugs 1999;8:2141–58.
57. Sohn YS, Breuer W, Munnich A, Cabantchik ZI. Redistribution of accumulated cell iron: a modality of chelation with therapeutic implications. Blood 2008;111:1690–9.
58. Cloonan SM, Glass K, Laucho-Contreras ME, Bhashyam AR, Cervo M, Pabón MA, et al. Mitochondrial iron chelation ameliorates cigarette smoke–induced bronchitis and emphysema in mice. Nat Med 2016;22:163–74.
59. Launonen I-M, Lyytikäinen N, Casado J, Anttila EA, Szabó A, Haltia U-M, et al. Single-cell tumor-immune microenvironment of BRCA1/2 mutated high-grade serous ovarian cancer. Nat Commun 2022;13:835.
60. Cummings M, Freer C, Orsi NM. Targeting the tumour microenvironment in platinum-resistant ovarian cancer. Semin Cancer Biol 2021;77:3–28.
61. Lukesova S, Vroblova V, Tosner J, Kopecky J, Sedlakova I, Čermáková E, et al. Comparative study of various subpopulations of cytotoxic cells in blood and ascites from patients with ovarian carcinoma. Contemp Oncol (Pozn) 2015;19:290–9.
62. Gonzalez VD, Huang Y-W, Delgado-Gonzalez A, Chen S-Y, Donoso K, Sachs K, et al. High-grade serous ovarian tumor cells modulate NK

cell function to create an immune-tolerant microenvironment. Cell Rep 2021;36:109632.
63. Agrawal S, Fox J, Thyagarajan B, Fox JH. Brain mitochondrial iron accumulates in Huntington's disease, mediates mitochondrial dysfunction, and can be removed pharmacologically. Free Radic Biol Med 2018;120:317–29.
64. Fiorillo M, Tóth F, Brindisi M, Sotgia F, Lisanti MP. Deferiprone (DFP) targets cancer stem cell (CSC) propagation by inhibiting mitochondrial metabolism and inducing ROS production. Cells 2020;9:1529.
65. Aibar S, González-Blas CB, Moerman T, Huynh-Thu VA, Imrichova H, Hulselmans G, et al. SCENIC: single-cell regulatory network inference and clustering. Nat Methods 2017;14:1083–6.
66. Sosinowski T, White JT, Cross EW, Haluszczak C, Marrack P, Gapin L, et al. CD8α+ dendritic cell trans presentation of IL-15 to naive CD8+ T cells produces antigen-inexperienced T cells in the periphery with memory phenotype and function. J Immunol 2013;190:1936–47.
67. Roby KF, Taylor CC, Sweetwood JP, Cheng Y, Pace JL, Tawfik O, et al. Development of a syngeneic mouse model for events related to ovarian cancer. Carcinogenesis 2000;21:585–91.
68. Paffenholz SV, Salvagno C, Ho Y-J, Limjoco M, Baslan T, Tian S, et al. Senescence induction dictates response to chemo- and immunotherapy in preclinical models of ovarian cancer. Proc Natl Acad Sci U S A 2022;119:e2117754119.
69. Andreatta M, Carmona SJ. UCell: robust and scalable single-cell gene signature scoring. Comput Struct Biotechnol J 2021;19:3796–8.
70. Hao Y, Hao S, Andersen-Nissen E, Mauck WM, Zheng S, Butler A, et al. Integrated analysis of multimodal single-cell data. Cell 2021;184:3573–87.e29.
71. Pauli C, Hopkins BD, Prandi D, Shaw R, Fedrizzi T, Sboner A, et al. Personalized *in vitro* and *in vivo* cancer models to guide precision medicine. Cancer Discov 2017;7:462–77.
72. Ianevski A, Giri AK, Aittokallio T. SynergyFinder 3.0: an interactive analysis and consensus interpretation of multi-drug synergies across multiple samples. Nucleic Acids Res 2022;50:W739–43.
73. Morrison GR. Fluorometric microdetermination of heme protein. Anal Chem 1965;37:1124–6.
74. Sassa S. Sequential induction of heme pathway enzymes during erythroid differentiation of mouse Friend leukemia virus-infected cells. J Exp Med 1976;143:305–15.